Computational Mechanics manuscript No.
(will be inserted by the editor)

ELASTIC LARGE DEFLECTION ANALYSIS OF PLATES SUBJECTED TO UNIAXIAL THRUST USING MESHFREE MINDLIN-REISSNER FORMULATION

SHOTA SADAMOTO · SATOYUKI TANAKA · SHIGENOBU OKAZAWA

Received: date / Accepted: date

Abstract A meshfree approach for plate buckling/post-buckling problems in the case of uniaxial thrust is presented. A geometrical nonlinear formulation is employed using reproducing kernel approximation and stabilized conforming nodal integration. The bending components are represented by Mindlin-Reissner plate theory. The formulation has a locking-free property in imposing the Kirchhoff mode reproducing condition. In addition, in-plane deformation components are approximated by reproducing kernels. The deformation components are coupled to solve the general plate bending problem with geometrical non-linearity. In buckling/post-buckling analysis of plates, the in-plane displacement of the edges in their perpendicular directions is assumed to be uniform by considering the continuity of plating, and periodic boundary conditions are considered in assuming the periodicity of structures. In such boundary condition enforcements, some node displacements/rotations should be synchronized with others. However, the enforcements introduce difficulties in the meshfree approach because the reproducing kernel function does not have the so-called Kronecker delta property. In this paper, the multiple point constraint technique is introduced to treat such boundary conditions as well as the essential boundary conditions. Numerical studies are performed to examine the accuracy of the multiple point constraint enforcements. As numerical examples, buckling/post-buckling analyses of a rectangular plate and stiffened plate structure are presented to validate the proposed approach.

Keywords Meshfree method · Reproducing kernel approximation · Large deflection analysis · Multiple Point Constraint

S. Sadamoto, S. Tanaka, S. Okazawa
Graduate School of Engineering, Hiroshima University, 4-1, Kagamiyama 1-chome, Higashi-Hiroshima 739-8527, Japan
Tel.: +81-82-424-7859
Fax: +81-82-422-8527
E-mail: d115754@hiroshima-u.ac.jp

S. Tanaka
E-mail: satoyuki@hiroshima-u.ac.jp

S. Okazawa
E-mail: okazawa@hiroshima-u.ac.jp

1 Introduction

In solid/structural analysis using meshfree methods, bodies are discretized according to distributed nodes, and deformations are represented by interpolation functions located at the nodes. The methodologies do not require finite element meshes in the discretization and therefore avoid difficulties of mesh distortion in large deformation analyses. So far, various meshfree methods have been proposed. The pioneering works of the meshfree method are the diffuse element method (DEM) [1], element free Galerkin method (EFGM) [2], reproducing kernel particle method (RKPM) [3], H-P Clouds [4] and meshless local Petrov-Galerkin (MLPG) method [5]. The moving least square (MLS) approximation or reproducing kernel (RK) approximation is sometimes used to generate the interpolation functions. In the past 20 years, there has been much research into the development of new meshfree methods, boundary treatment techniques and discretization for solving science and engineering problems. The meshfree/particle methods are summarized in [6] [7] [8] [9] [10].

Transportation vehicles, such as ships, aircraft and railcars, are very large structures composed of thin-

plates. When axial compressive stress in the in-plane direction acts on the structure and reaches a critical value, the structural members undergo buckling. The deflection begins to increase in addition to the in-plane displacement after the buckling. In assessing the integrity and reliability of the structures, buckling/post-buckling behaviors of the structural members are important. Although direct approaches for three-dimensional continuum using meshfree analyses have been adopted for thin-plate/shell structures [11] [12] [13], structural modeling based on a classical beam or plate theory is useful, as are finite element methods (FEMs), from the viewpoint of computational efficiency. Researchers have attempted to analyze plate/shell structures with meshfree methods. Krysl and Belytschko firstly solved plate [14] and shell [15] problems using the EFGM. Long and Atluri solved the thin-plate bending problem using the MLPG method [16]. Wang and Chen solved the Mindlin-Reissner plate theory using the RKPM with stabilized conforming nodal integration (SCNI) [17] and the thin-plate bending problem using the Hermite reproducing kernel (HRK) and sub-domain stabilized conforming integration (SSCI) [18] [19] [20]. Chen and Wang also developed shear deformable shells in Cartesian coordinates using the RKPM [21]. The Kirchhoff plate problem was solved by Liu et al. [22] using a meshfree Hermite-type radial point interpolation method. Noguchi et al. carried out geometrical nonlinear analyses for shell and spatial structures using the EFGM [23], and Wang et al. solved the problem of shear deformable plates with geometrical nonlinearity with RKs and SCNI [24]. Elastic buckling analysis of plates and corrugated plates using a meshfree approach has been carried out, employing eigenvalue analyses to evaluate the buckling loads and buckling modes [25] [26] [27]. Liew et al. [28] developed a geometrical nonlinear approach for folded plate structures. An adaptive enrichment meshfree approach was presented by Lu et al. [29] to evaluate the buckling and post-buckling behaviors in sheet metal forming. Rabczuk et al. [30] solved the problem of arbitrarily evolving cracks in a thin-shell structure considering nonlinear dynamic fracture phenomena using the EFGM.

In this study, large deflection analysis of plate structures is presented to evaluate buckling and post-buckling behaviors using RK approximation. A geometrical nonlinear formulation of plate bending problems considering in-plane deformations is developed. The bending components are represented by Mindlin-Reissener plate theory proposed by Wang et al. [17]. The formulation includes the shear deformable effect and has a locking-free property for imposing the Kirchhoff mode reproducing condition (KMRC) with pure bending mode. The properties are satisfied by employing more than complete quadratic bases in the construction of RKs. In addition, in-plane deformations are approximated using RK approximation. They are coupled and formulated using the total Lagrangian formulation to solve the general plate bending problem with geometrical nonlinearity. Each node has five degrees of freedoms (DOFs). The model is discretized with a Voronoi cell diagram [31], and the tangent stiffness matrix is numerically integrated through SCNI [32] [33] and SSCI [18] to eliminate spatial instability in nodal integration.

In buckling analysis of plates under uniaxial thrust, the in-plane displacement of the edges in their perpendicular direction is assumed to be uniform in considering the continuity of the plating. In addition, a periodic boundary condition (BC) is considered in assuming periodicity of the structures. In such BCs, some node displacements/rotations should be synchronized with others. However, the enforcements introduce difficulties in the meshfree approaches because the RK function does not have the so-called Kronecker delta property. So far, techniques have been adopted to treat BCs and contact problems; e.g., Lagrange multipliers [2], penalty methods [23] [34], coupling with the conventional FEM [35] [36] [37], the full transformation method [38], the mixed transformation method and the boundary singular kernel method [39]. In this study, the multiple point constraint (MPC) technique is introduced to assume continuity of plating and periodicity of structures. The enforcements can be consistently discussed the essential BC enforcements as well. Nevertheless, the MPC technique is a simple and efficient approach for enforcing BCs in FEMs, and it should be considered when adopting a meshfree approach because the RKs have a compact support property. In this work, we investigate the MPC technique and find that the approach does not exactly pass the so-called patch test. We then propose an approach to improve the accuracy of the solution. Although it is possible for BCs to be enforced by other enforcement approaches, the MPC technique is free from the ill-condition of the tangent stiffness matrix and there are no additional DOFs in terms of the enforcements. Nagashima [40] adopted MPC enforcements to treat essential BCs in two-dimensional EFGM analyses, and researchers [41][42] have employed the approach to treat the periodic BC of rubber materials. There have been a few discussions and reports of employing MPC techniques in taking a meshfree approach and in plate buckling/post-buckling analyses assuming continuity of plates and periodicity of the structures. As numerical examples, buckling/post-buckling analyses of plates and stiffened plates subject to uni-axial

thrust are demonstrated to validate the proposed approach.

The layout of this paper is as follows. A geometrical nonlinear formulation using RK approximation for the plate bending problem considering in-plane deformation is presented in Chapter 2. An MPC technique for enforcing continuity of plating and periodicity of structures is presented in Chapter 3. Chapter 4 demonstrates the buckling/post-buckling analysis of plates and stiffened plates as the numerical examples. Finally, concluding remarks are given in Chapter 5.

2 Geometrical nonlinear formulation for the plate bending problem

2.1 Representation of a plate deformation

Fig. 1 (a) is a schematic illustration of a plate bending problem. The surface area of the plate is S, the plate thickness is t_h and the plate volume is $V(= S \times t_h)$. The plate boundary is denoted L. A discretization of the plate adopting a meshfree approach is shown in Fig. 1 (b). The nodes are distributed in the middle surface of the plate. Meshfree interpolation functions are generated on nodes located in the support area. In buckling/post-buckling analyses of the plate under uni-axial thrust, membrane deformations are not insignificant compared with the bending components. A geometrical nonlinear plate bending formulation is employed considering in-plane deformations. In this formulation, two DOFs (u_1^p, u_2^p) plus three DOFs (w, β_1, β_2) are considered per node. u_1^p and u_2^p are in-plane displacements in x_1 and x_2 directions, w is the deflection component of the plate, and β_1 and β_2 are deflection angles relative to the x_1 and x_2 axes as shown in Fig. 1 (a). The DOFs of a node are illustrated in Fig. 1 (c). To describe general plate deformation, in-plane deformation and bending components are coupled. The displacement vector $\boldsymbol{u}(\boldsymbol{x})$ for a plate is represented as

$$\boldsymbol{u}(\boldsymbol{x}) = \begin{Bmatrix} u_1 \\ u_2 \\ u_3 \end{Bmatrix} = \begin{Bmatrix} u_1^p - z\beta_1 \\ u_2^p - z\beta_2 \\ w \end{Bmatrix}, \tag{1}$$

where $u_i (i = 1, 2, 3)$ represents plate displacement along the $x_i (i = 1, 2, 3)$ axis. z $(|z| \leq t_h/2)$ represents the plate thickness direction. The deflection angles β_1 and β_2 are obtained according to Mindlin-Reissner plate theory:

$$\beta_1 = \frac{\partial w}{\partial x_1} - \gamma_1, \qquad \beta_2 = \frac{\partial w}{\partial x_2} - \gamma_2, \tag{2}$$

where $\gamma_i (i = 1, 2)$ denotes the shear strains in the x_1 and x_2 directions.

2.2 Reproducing kernel approximation

Let the middle surface in Fig. 1 (a) be discretized by a set of NP nodes $(\boldsymbol{x}_1, \cdots, \boldsymbol{x}_I, \cdots, \boldsymbol{x}_{NP})$ as shown in Fig. 1(b). Hereafter, the in-plane (membrane) components (u_1^p, u_2^p) and bending components (w, β_1, β_2) are denoted $\{ u_1^p \; u_2^p \; w \; \beta_1 \; \beta_2 \} = \{ v_1 \; v_2 \; v_3 \; v_4 \; v_5 \}$ for simplicity of description. In this approach, the vectors $v_i^h(\boldsymbol{x}) (i = 1, \cdots, 5)$ are represented by RKs $\psi_I(\boldsymbol{x})$ $(I = 1, \cdots, NP)$:

$$v_i^h(\boldsymbol{x}) = \sum_{I=1}^{NP} \psi_I(\boldsymbol{x}) v_{iI}, \qquad (i = 1, \cdots, 5) \tag{3}$$

where v_{iI} denotes the coefficient vectors corresponding to displacement/rotational components. The RK function $\psi_I(\boldsymbol{x})$ is constructed as the sum of the original kernel function $\phi_{aI}(\boldsymbol{x})$ so as to satisfy the so-called consistency condition [43]. The RK function $\psi_I(\boldsymbol{x})$ is represented using a basis vector $\boldsymbol{h}(\boldsymbol{x})$ and coefficient vector $\boldsymbol{b}(\boldsymbol{x})$:

$$\psi_I(\boldsymbol{x}) = \boldsymbol{h}^T(\boldsymbol{x}_I - \boldsymbol{x}) \boldsymbol{b}(\boldsymbol{x}) \phi_{aI}(\boldsymbol{x}_I - \boldsymbol{x}). \tag{4}$$

Complete quadratic bases are used as the basis vector in this formulation; *i.e.*, $\boldsymbol{h}^T(\boldsymbol{x}) = \{ 1 \; x_1 \; x_2 \; x_1^2 \; x_1 x_2 \; x_2^2 \}$. And, $\boldsymbol{b}^T(\boldsymbol{x}) = \{ b_{00} \; b_{10} \; b_{01} \; b_{20} \; b_{11} \; b_{02} \}$ is the coefficient vector of the RK function. So far, several functions have been proposed as the original kernel function [7][9]. For example, the cubic spline kernel function is written as

$$\phi_{aI}(\boldsymbol{x}_I - \boldsymbol{x}, h) = \frac{10}{7\pi h^2} \begin{cases} 1 - \frac{3}{2}s^2 + \frac{3}{4}s^3 & (0 \leq s \leq 1) \\ \frac{1}{4}(2-s)^3 & (1 \leq s \leq 2) \\ 0 & (2 \leq s) \end{cases}, \tag{5}$$

where $s(=|\boldsymbol{x}_I - \boldsymbol{x}|/h)$ is the normalized distance from the center of the kernel and h is a parameter that determines the function support.

The consistency condition in the two-dimensional case is expressed as

$$\sum_{I=1}^{NP} \psi_I(\boldsymbol{x}) x_{1I}^i x_{2I}^j = x_1^i x_2^j, \quad (0 \leq i + j \leq 2). \tag{6}$$

Eq. (6) can be rewritten as the following vector form:

$$\sum_{I=1}^{NP} \psi_I(\boldsymbol{x}) \boldsymbol{h}(\boldsymbol{x}_I - \boldsymbol{x}) = \boldsymbol{h}(\boldsymbol{0}). \tag{7}$$

Substituting eq.(4) into eq.(7), a simultaneous linear equation is obtained:

$$\boldsymbol{M}(\boldsymbol{x}) \boldsymbol{b}(\boldsymbol{x}) = \boldsymbol{h}(\boldsymbol{0}), \tag{8}$$

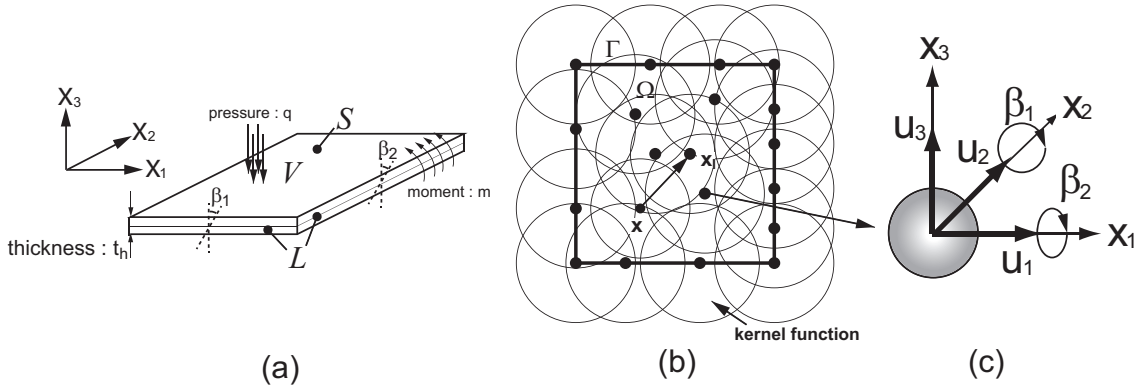

Fig. 1 Implementation of a meshfree method for a plate bending problem [(a) Plate model to be solved, (b) A meshfree discretization of the plate, (c) Five DOFs per node]

where $\boldsymbol{M}(\boldsymbol{x})$ is a moment matrix, written as

$$\boldsymbol{M}(\boldsymbol{x}) = \sum_{I=1}^{NP} \boldsymbol{h}(\boldsymbol{x}_I - \boldsymbol{x})\boldsymbol{h}^T(\boldsymbol{x}_I - \boldsymbol{x})\phi_{aI}(\boldsymbol{x}_I - \boldsymbol{x}). \tag{9}$$

We can obtain the coefficient vector $\boldsymbol{b}(\boldsymbol{x})$ by solving eq.(8). The equation (4) can be rewritten as

$$\psi_I(\boldsymbol{x}) = \boldsymbol{h}^T(\boldsymbol{0})\boldsymbol{M}^{-1}(\boldsymbol{x})\boldsymbol{h}(\boldsymbol{x}_I - \boldsymbol{x})\phi_{aI}(\boldsymbol{x}_I - \boldsymbol{x}). \tag{10}$$

The deformation of the plate expressed by eq.(1) can be represented in matrix form:

$$\boldsymbol{u}^h(\boldsymbol{x}) = \sum_{I=1}^{NP} \boldsymbol{N}_I \boldsymbol{V}_I, \tag{11}$$

where $\boldsymbol{u}^h(\boldsymbol{x})$ is a displacement vector, $\boldsymbol{N}_I$ is a matrix of RKs regarding the displacement and rotational components, and $\boldsymbol{V}_I$ denotes their coefficient vectors. These terms are expressed as

$$\boldsymbol{u}^h = \left\{ u_1^h \; u_2^h \; u_3^h \right\}^T, \tag{12}$$

$$\boldsymbol{N}_I = \begin{bmatrix} \psi_I & 0 & 0 & -z\psi_I & 0 \\ 0 & \psi_I & 0 & 0 & -z\psi_I \\ 0 & 0 & \psi_I & 0 & 0 \end{bmatrix}, \tag{13}$$

$$\boldsymbol{V}_I = \left\{ v_{1I} \; v_{2I} \; v_{3I} \; v_{4I} \; v_{5I} \right\}^T. \tag{14}$$

In plate bending formulation, the so-called KMRC [17] [18] should be satisfied to solve thin-plate deformation. The pure bending mode $\bar{w}_I$ is expressed by quadratic polynomial:

$$\bar{w}_I = \sum_{i+j=0}^{2} c_{ij} x_{I1}^i x_{I2}^j, \tag{15}$$

where c_{ij} is an arbitrary constant and I express the I-th node. Angles $\bar{\beta}_{I1}$ and $\bar{\beta}_{I2}$ are expressed by partial derivatives of $\bar{w}_I$:

$$\bar{\beta}_{I1} = \sum_{i+j=1}^{2} i c_{ij} x_{I1}^{(i-1)} x_{I2}^j, \tag{16}$$

$$\bar{\beta}_{I2} = \sum_{i+j=1}^{2} j c_{ij} x_{I1}^i x_{I2}^{(j-1)}. \tag{17}$$

Here, the KMRC can be expressed as properties of the approximates of curvature $\bar{\kappa}_{Iij}^h$ and shear strain $\bar{\gamma}_{Ii}^h$:

$$\bar{\kappa}_{Iij}^h = \sum_{I=1}^{NP} \frac{1}{2} \left(\psi_{I,j}\bar{\beta}_{Ii} + \psi_{I,i}\bar{\beta}_{Ij} \right) = \text{const.}, \tag{18}$$

$$\bar{\gamma}_{Ik}^h = \sum_{I=1}^{NP} \left(\psi_{I,k}\bar{w}_I - \psi\bar{\beta}_{Ik} \right) = 0, \tag{19}$$

where $\{i,j\} = \{1,2\}$, $k = \{1,2\}$,

where $\psi_{I,i}$ $(i = 1,2)$ denotes partial derivatives of ψ_I. According to the literature [17], it follows from eqs. (18) and (19) that

$$\sum_{I=1}^{NP} \psi_{I,i} \left[(x_1^k x_2^l)_{,j} \right]_I = (x_1^k x_2^l)_{,ij} = \text{const.}, \tag{20}$$

for $k + l = 0, 1, 2$.

Table 1 gives the error norms between the exact modes and approximates. 11×11 regularly distributed nodes are considered. The basis vectors are

$$\boldsymbol{h}_L^T = \{ 1 \; x_1 \; x_2 \}, \tag{21}$$

$$\boldsymbol{h}_{BL}^T = \{ 1 \; x_1 \; x_2 \;\; x_1 x_2 \}, \tag{22}$$

$$\boldsymbol{h}_Q^T = \{ 1 \; x_1 \; x_2 \; x_1^2 \; x_1 x_2 \; x_2^2 \}, \tag{23}$$

where $\boldsymbol{h}_L$, $\boldsymbol{h}_{BL}$ and $\boldsymbol{h}_Q$ are linear, bi-linear and complete quadratic bases, respectively. The components in Table 1; (i) pure bending mode $\bar{w}_I$, (ii) derivative $\partial\bar{w}_I/\partial x_1$ and (iii) derivative $\partial\bar{w}_I/\partial x_2$ are considered. When the RK shape function is once differentable, eq. (20) is satisfied. However, if the basis vector is less than the complete quadratic, the pure bending mode and its derivatives cannot be represented exactly as shown in Table 1. The complete quadratic is thus applied in this study.

Table 1 Error norms of the pure bending mode

	(i)	(ii)	(iii)
Linear	7.84E+00	9.52E-01	9.52E-01
Bi-linear	2.79E+00	8.53E-01	8.53E-01
Quadratic	1.59E-14	7.53E-15	8.59E-15

2.3 A geometrical nonlinear formulation

A total Lagrangian formulation is used to describe the large deflection of a plate. Green-Lagrange strains and second Piola-Kirchhoff stresses are used to express the principle of virtual work. The virtual work at time $t' = t + \Delta t$ can be expressed as

$$\int_V {}_0^{t'}\boldsymbol{S} : \delta {}_0^{t'}\boldsymbol{E} dV = {}^{t'}\delta R,$$
$${}^{t'}\delta R = \int_{S_t} {}_0^{t'}\bar{\boldsymbol{t}} \cdot \delta \boldsymbol{u} dS, \tag{24}$$

where ${}_0^{t'}\boldsymbol{S}$ and ${}_0^{t'}\boldsymbol{E}$ are the second Piola-Kirchhoff stress tensor and Green-Lagrange strain tensor, respectively at time t', which refers to the initial configuration. The terms with δ are variational components. ${}^{t'}\delta R$ is the virtual work of the external force; V is the volume of the analysis domain; and ${}_0^{t'}\bar{\boldsymbol{t}}$ is the traction force vector for the traction boundary S_t at time t'. To derive the tangent stiffness matrix for the incremental nonlinear analysis, the virtual work principle is decomposed according to linear relations of the displacement vector at time t' : ${}^{t'}\boldsymbol{u} = {}^{t}\boldsymbol{u} + \boldsymbol{u}$, where ${}^{t}\boldsymbol{u}$ is the displacement vector at time t, and $\boldsymbol{u}$ is the increment from time t to t'. The Green-Lagrange strain tensor is ${}_0^{t'}\boldsymbol{E} = {}_0^{t}\boldsymbol{E} + {}_0\boldsymbol{E}_L + {}_0\boldsymbol{E}_{NL}$ and the second Piola-Kirchhoff stress tensor is ${}_0^{t'}\boldsymbol{S} = {}_0^{t}\boldsymbol{S} + {}_0\boldsymbol{S}$. Therefore, eq. (24) can be rewritten as

$$\int_V {}_0\boldsymbol{S} : (\delta_0\boldsymbol{E}_L + \delta_0\boldsymbol{E}_{NL}) dV + \int_V {}_0^{t}\boldsymbol{S} : \delta_0\boldsymbol{E}_{NL} dV$$
$$= {}^{t'}\delta R - \int_V {}_0^{t}\boldsymbol{S} : \delta_0\boldsymbol{E}_L dV, \tag{25}$$

where ${}_0\boldsymbol{E}_L$ and ${}_0\boldsymbol{E}_{NL}$ are the linear and nonlinear parts of the Green-Largange strain increment. ${}_0\boldsymbol{S}$ is the second Piola-Kirchhoff stress increment from time t to t'. The left-hand side of eq. (25) can be linearized:

$$\lim_{\Delta t \to 0} \{\text{left hand side of eq. (25)}\} / \Delta t$$
$$= \int_V {}_0^{t}\dot{\boldsymbol{S}} : \delta_0\boldsymbol{E}_L dV + \int_V {}_0^{t}\boldsymbol{S} : (\delta_0\dot{\boldsymbol{E}}_{NL}) dV, \tag{26}$$

where the term ${}_0\boldsymbol{S} : \delta\boldsymbol{E}_{NL}$ is more than the second-order of $\boldsymbol{u}$. It can be ignored because $\boldsymbol{u} \to 0$ when $\Delta t \to 0$. Additionally, $\dot{\cdot}$ denotes a material time derivative. Finally, we obtain a linearized equation for the virtual work principle of eq. (25):

$$\left[\int_V {}_0^{t}\dot{\boldsymbol{S}} : \delta_0\boldsymbol{E}_L dV + \int_V {}_0^{t}\boldsymbol{S} : (\delta_0\dot{\boldsymbol{E}}_{NL}) dV\right] \Delta t$$
$$= {}_0^{t'}\delta R - \int_V {}_0^{t}\boldsymbol{S} : \delta_0\boldsymbol{E}_L dV. \tag{27}$$

In this study, the MPC technique is adopted to assume the continuity of plating and periodicity of structures as well as the essential BCs. They are included as a constraint condition in the weak form. The next chapter presents the MPC technique and implementation.

2.4 Nodal integration

In the meshfree formulation, SCNI [32][33] and SSCI [18][19][20] are introduced as the numerical integration of the tangent stiffness matrix of eq. (27). The numerical integration techniques satisfy the so-called integration constraint (IC), which is a necessary condition for linear exactness in the Galerkin-based meshfree method. In addition, numerical instabilities due to a spurious mode of the tangent stiffness matrix composed by using direct nodal integration can be avoided. In SCNI and SSCI, the strain components are smoothed using the Gauss divergence theorem. Nodes are dispersed on the plate as shown in Fig. 2 (a). $\boldsymbol{x}_K$ is the coordinate of the K-th node.

2.4.1 SCNI

The discretized model of Fig. 2 (a) employing SCNI is shown in Fig. 2 (b). A Voronoi cell diagram [31] is adopted to automate the generation of the model. Each node is surrounded by a Voronoi cell. The area within the solid line Γ_K is Ω_K. $\boldsymbol{n}$ is a normal vector of Ω_K. In SCNI, differentiations of the displacement/rotational components $v^h_{i,j}(\boldsymbol{x}_K)$ are represented as

$$\begin{aligned} v^h_{i,j}(\boldsymbol{x}_K) &= \frac{1}{A_K}\int_{\Omega_K} v^h_{i,j}(\boldsymbol{x}_K) d\Omega \\ &= \frac{1}{A_K}\int_{\Gamma_K} v^h_i(\boldsymbol{x}_K) n_j d\Gamma \\ &= \sum_{I=1}^{NP} \frac{1}{A_K}\int_{\Gamma_K} \psi_I(\boldsymbol{x}_K) n_j v_{iI} d\Gamma \\ &= \sum_{I=1}^{NP} b_{Ij}(\boldsymbol{x}_K) v_{iI}, \\ \text{where } & i = \{1,2,3,4,5\},\ j = \{1,2\}. \end{aligned} \tag{28}$$

The scalar value $b_{Ii}(\boldsymbol{x}_K)$ is represented as

$$b_{Ii}(\boldsymbol{x}_K) = \frac{1}{A_K}\int_{\Gamma_K} \psi_I(\boldsymbol{x}_K) n_i d\Gamma, \quad i = \{1,2\}, \tag{29}$$

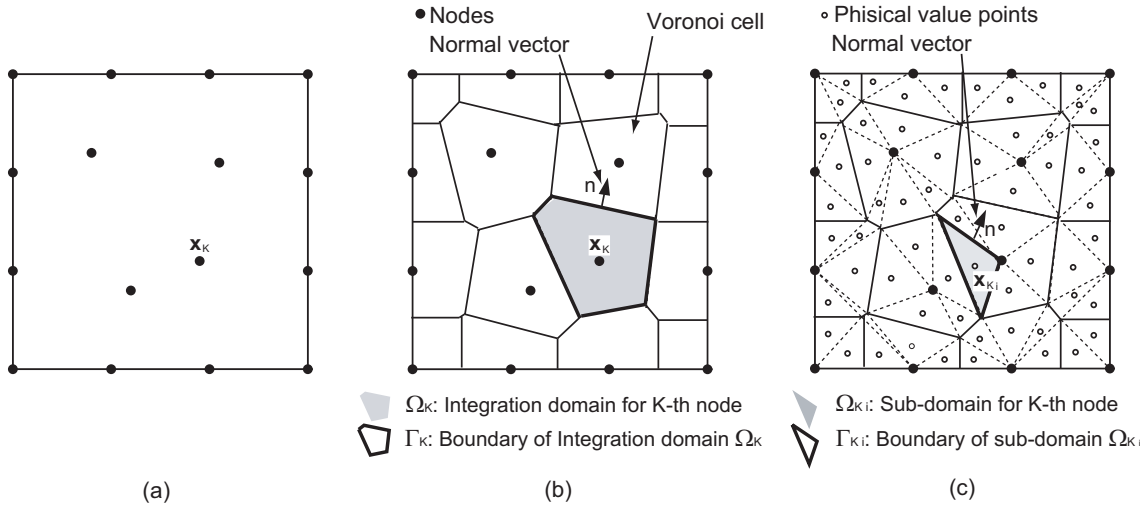

Fig. 2 Discretization of a rectangular plate using nodes [(a) Distributed nodes on a plate, (b) SCNI with a Voronoi cell diagram, (c) SSCI with a sub-domain of the Voronoi cell]

where A_K is the area of Ω_K, n_i $(i = 1, 2)$ denotes the x_1 and x_2 components of the normal vector of the boundary Γ_K. Gauss quadrature is performed in the line integration of eq.(29).

2.4.2 SSCI

SSCI is also introduced to effectively integrate the stiffness matrix. SCNI is basically adopted in the numerical integration, but the Voronoi cell is further divided to accurately integrate the stiffness matrix where high gradients of displacements/stresses are located. The discretization model of Fig. 2 (a) using SSCI is shown in Fig. 2 (c). Ω_K in Fig. 2 (b) is divided using triangular domains Ω_{K_i}. $\boldsymbol{x}_{K_i}$ is the center of gravity of the triangulation, the point have stress/strain components values. In SSCI, the differentiations of displacement/rotational components $v^h_{j,k}(\boldsymbol{x}_{K_i})$ are expressed as

$$\begin{aligned} v^h_{j,k}(\boldsymbol{x}_{K_i}) &= \frac{1}{A_{K_i}} \int_{\Omega_K} v^h_{j,k}(\boldsymbol{x}_{K_i}) d\Omega \\ &= \frac{1}{A_{K_i}} \int_{\Gamma_{K_i}} v^h_j(\boldsymbol{x}_{K_i}) n_k d\Gamma \\ &= \sum_{I=1}^{NP} \frac{1}{A_{K_i}} \int_{\Gamma_{K_i}} \psi_I(\boldsymbol{x}_K) n_k v_{jI} d\Gamma \\ &= \sum_{I=1}^{NP} b_{Ik}(\boldsymbol{x}_{K_i}) v_{jI}, \\ \text{where } \ j &= \{1, 2, 3, 4, 5\}, \ k = \{1, 2\}. \end{aligned} \tag{30}$$

The scalar value $b_{Ij}(\boldsymbol{x}_{K_i})$ is expressed as

$$b_{Ij}(\boldsymbol{x}_{K_i}) = \frac{1}{A_{K_i}} \int_{\Gamma_{K_i}} \psi_I(\boldsymbol{x}_{K_i}) n_j d\Gamma, \quad j = \{1, 2\}, \tag{31}$$

where A_{K_i} is the area of Ω_{K_i}, n_i $(i = 1, 2)$ denotes the x_1 and x_2 components of the normal vector of the boundary Γ_{K_i}. Gauss quadrature is performed on the line integration of eq.(31).

2.5 Discretization of the weak form

The virtual work of the principle as shown in eq. (27) is discretized through RK approximation, SCNI and SSCI. The displacement at time t : ${}^t\boldsymbol{u}^h(\boldsymbol{x})$ is given by eq. (11). The Green-Lagrange strain components at time t can be written as

$$\begin{aligned} &\left\{ {}_0E_{L11} \ {}_0E_{L22} \ 2{}_0E_{L12} \ 2{}_0E_{L31} \ 2{}_0E_{L23} \right\}^T \\ &= \sum_{I=1}^{NP} {}^t_0\boldsymbol{B}_{LI} \boldsymbol{V}_I, \end{aligned} \tag{32}$$

where the matrix ${}^t_0\boldsymbol{B}_{LI}$ is the linear part of the Green-Lagrange strain increment for the I-th node. The components can be represented in matrix form as

$${}^t_0\boldsymbol{B}_{LI} = \begin{bmatrix} b_{I1}F_{11} & b_{I1}F_{21} & b_{I1}F_{31} \\ b_{I2}F_{12} & b_{I2}F_{22} & b_{I2}F_{32} \\ b_{I1}F_{12} + b_{I2}F_{11} & b_{I1}F_{22} + b_{I2}F_{21} & b_{I1}F_{32} + b_{I2}F_{31} \\ \psi_{I,1}F_{13} & \psi_{I,1}F_{23} & \psi_{I,1} \\ \psi_{I,2}F_{13} & \psi_{I,2}F_{23} & \psi_{I,2} \end{bmatrix}$$
$$\begin{bmatrix} -zb_{I1}F_{11} & -zb_{I1}F_{21} \\ -zb_{I2}F_{12} & -zb_{I2}F_{22} \\ -z(b_{I1}F_{12} + b_{I2}F_{11}) & -z(b_{I1}F_{22} + b_{I2}F_{21}) \\ -\psi_I F_{11} & -\psi_I F_{21} \\ -\psi_I F_{12} & -\psi_I F_{22} \end{bmatrix}, \tag{33}$$

where $b_{Ii}(i=1,2)$ denotes the line integrations with SCNI as shown in eq. (29) or with SSCI as shown in eq. (31) , ψ_I are RKs, and $\psi_{I,i}(i=1,2)$ denotes differentiation of RKs for the I-th node. F_{ij} denotes deformation gradient tensors and is expressed as

$$F_{ij} = \delta_{ij} + \frac{\partial^t u_i^h}{\partial X_j}, \tag{34}$$

where $\partial^t u_i^h/\partial X_j$ is the differentiation of displacements ${}^t u_i^h(\boldsymbol{x})$ in terms of coordinate systems of initial configuration X_j $(j=1,2,3)$. In the derivation of eq. (33), deflection angle components are ignored since they are assumed to be smaller than the other terms. The deformation gradient tensors F_{ij} are derived with SCNI in a previous step. In a similar manner, the nonlinear part of strain increments ${}^t_0\boldsymbol{B}_{NLI}$ for the I-th node are expressed as

$$\left\{ \boldsymbol{u}_{,1}^{hT} \ \boldsymbol{u}_{,2}^{hT} \ \boldsymbol{u}_{,3}^{hT} \right\}^T = \sum_{I=1}^{NP} {}^t_0\boldsymbol{B}_{NLI}\boldsymbol{V}_I, \tag{35}$$

where $\boldsymbol{u}_{,i}^{hT}(i=1,2,3)$ denotes vectors in terms of the differentiation of displacements $u_{,i}^h$ $(i=1,2,3)$:

$$\boldsymbol{u}_{,i}^{hT} = \left\{ u_{1,i}^h \quad u_{2,i}^h \quad u_{3,i}^h \right\}, \quad i = \{1,2,3\}. \tag{36}$$

The matrix ${}^t_0\boldsymbol{B}_{NLI}$ is composed from $b_{Ii}(i=1,2)$ and RKs ψ_I:

$${}^t_0\boldsymbol{B}_{NLI} = \begin{bmatrix} b_{I1} & 0 & 0 & -zb_{I1} & 0 \\ 0 & b_{I1} & 0 & 0 & -zb_{I1} \\ 0 & 0 & b_{I1} & 0 & 0 \\ b_{I2} & 0 & 0 & -zb_{I2} & 0 \\ 0 & b_{I2} & 0 & 0 & -zb_{I2} \\ 0 & 0 & b_{I2} & 0 & 0 \\ 0 & 0 & 0 & -\psi_I & 0 \\ 0 & 0 & 0 & 0 & -\psi_I \\ 0 & 0 & 0 & 0 & 0 \end{bmatrix}. \tag{37}$$

Substituting matrices ${}^t_0\boldsymbol{B}_L$ and ${}^t_0\boldsymbol{B}_{NL}$ into eq.(27), the stiffness equation from time t to t' is obtained:

$${}^t_0\boldsymbol{K}\boldsymbol{V} = {}^{t'}_0\boldsymbol{F} - {}^t_0\boldsymbol{Q}, \tag{38}$$

where ${}^t_0\boldsymbol{K}$ is the stiffness matrix, ${}^t_0\boldsymbol{Q}$ is the internal force vector and ${}^{t'}_0\boldsymbol{F}$ is the external force vector at time t'. Their components are expressed as

$${}^t_0\boldsymbol{K}_{IJ} = {}^t_0\boldsymbol{K}_{L\,IJ} + {}^t_0\boldsymbol{K}_{NL\,IJ}, \tag{39}$$

$${}^t_0\boldsymbol{K}_{L\,IJ} = \sum_{K=1}^{NP} {}^t_0\boldsymbol{B}_{L\,I}^T(\boldsymbol{x}_K)\boldsymbol{D}\,{}^t_0\boldsymbol{B}_{L\,J}(\boldsymbol{x}_K)A_K, \tag{40}$$

$${}^t_0\boldsymbol{K}_{NL\,IJ} = \sum_{K=1}^{NP} {}^t_0\boldsymbol{B}_{NL\,I}^T(\boldsymbol{x}_K)\,{}^t_0\bar{\boldsymbol{S}}(\boldsymbol{x}_K)\,{}^t_0\boldsymbol{B}_{NL\,J}(\boldsymbol{x}_K)A_K, \tag{41}$$

$${}^t_0\boldsymbol{Q}_I = \sum_{K=1}^{NP} {}^t_0\boldsymbol{B}_{L\,I}^T(\boldsymbol{x}_K)\,{}^t_0\hat{\boldsymbol{S}}(\boldsymbol{x}_K)A_K. \tag{42}$$

${}^t_0\boldsymbol{K}_L$ and ${}^t_0\boldsymbol{K}_{NL}$ are the initial displacement term and initial stress term of the stiffness matrix ${}^t_0\boldsymbol{K}$. A_K is the area of Ω_K as shown in Fig. 2 (b). In this analysis, the plate is elastic material and a plane stress condition is assumed in the in-plane deformation. The stress-strain relation is derived as

$$\boldsymbol{D} = \frac{E}{1-\nu^2}\begin{bmatrix} 1 & \nu & 0 & 0 & 0 \\ \nu & 1 & 0 & 0 & 0 \\ 0 & 0 & \frac{1-\nu}{2} & 0 & 0 \\ 0 & 0 & 0 & \kappa\frac{1-\nu}{2} & 0 \\ 0 & 0 & 0 & 0 & \kappa\frac{1-\nu}{2} \end{bmatrix}, \tag{43}$$

where κ is the shear correction factor; $\kappa = \pi^2/12$ is adopted. E is Young's modulus and ν is Poisson's ratio. Matrix ${}^t_0\bar{\boldsymbol{S}}$ in eq. (41) is expressed using second Piola-Kirchhoff stress components as

$${}^t_0\bar{\boldsymbol{S}} = \begin{bmatrix} {}^t_0S_{11}\boldsymbol{I} & {}^t_0S_{12}\boldsymbol{I} & {}^t_0S_{13}\boldsymbol{I} \\ {}^t_0S_{21}\boldsymbol{I} & {}^t_0S_{22}\boldsymbol{I} & {}^t_0S_{23}\boldsymbol{I} \\ {}^t_0S_{31}\boldsymbol{I} & {}^t_0S_{32}\boldsymbol{I} & {}^t_0S_{33}\boldsymbol{I} \end{bmatrix}, \tag{44}$$

where $\boldsymbol{I}$ is a 3×3 unit vector. Additionally, vector ${}^t_0\hat{\boldsymbol{S}}$ in eq. (42) is expressed as

$${}^t_0\hat{\boldsymbol{S}}^T = \left\{ {}^t_0S_{11}\ {}^t_0S_{22}\ {}^t_0S_{33}\ {}^t_0S_{12}\ {}^t_0S_{23}\ {}^t_0S_{31} \right\}. \tag{45}$$

Because the deformation along the thickness direction is not considered, the stress component ${}^t_0S_{33}$ is assumed to be zero. In this formulation, the integration in the plate thickness direction is performed analytically as

$$\int_V \cdots dV = t_h \int_S \cdots dS \tag{46}$$

$$\int_V z \cdots dV = 0 \tag{47}$$

$$\int_V z^2 \cdots dV = \frac{t_h^3}{12}\int_S \cdots dS. \tag{48}$$

The linearized eq.(38) is solved from time t to $t+\Delta t$. The Newton-Raphson method is adopted to obtain the solution at time t'.

3 Treatment of BCs employing the MPC technique

In the preliminary stage, we follow the MPC technique for enforcing essential BCs in a meshfree approach [40], and the technique is extended to adopting BCs assuming continuity of plating and periodicity of structures. A two-dimensional rectangular plate is used to describe the problems as shown in Fig. 3(a). The left edge and underside edge are enforced as essential BCs. In-plane displacement of the right edge in the perpendicular direction is assumed to be uniform. The prescribed force

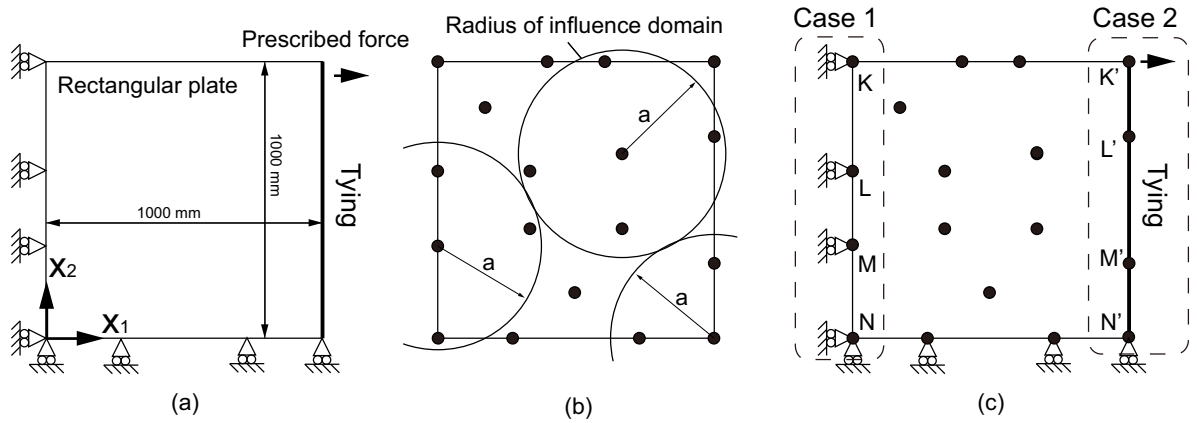

Fig. 3 Schematic illustrations of the two-dimensional rectangular plate model [(a) Dimensions of the rectangular plate model, (b) Meshfree discretization, (c) BC enforcement using the MPC technique]

is also enforced on the right edge. Numerical tests are performed to examine the MPC technique using this model. Only in-plane deformations are treated for simplicity of discussion, but the technique can easily be extended to plate bending problems that have rotational components. Verification for the plate bending problems is presented in numerical examples. In large deflection analyses of plates, the support size of the kernel functions is set to be uniform.

3.1 Enforcement of essential BCs

Essential BC enforcements using the MPC technique are presented. Here, we treat the enforcement on the left edge of the rectangular plate (Case 1) as shown in Fig. 3(c). We denote the four nodes along the edge as K, L, M and N. The positions are $\boldsymbol{x}_K$, $\boldsymbol{x}_L$, $\boldsymbol{x}_M$ and $\boldsymbol{x}_N$ respectively. The displacement in the x_1 direction can be represented by RKs as

$$v^h_{1K} = \sum_{I=1}^{NP} \psi_I(\boldsymbol{x}_K) v_{1I}, \quad v^h_{1L} = \sum_{I=1}^{NP} \psi_I(\boldsymbol{x}_L) v_{1I},$$
$$v^h_{1M} = \sum_{I=1}^{NP} \psi_I(\boldsymbol{x}_M) v_{1I}, \quad v^h_{1N} = \sum_{I=1}^{NP} \psi_I(\boldsymbol{x}_N) v_{1I}, \tag{49}$$

where RKs $\psi_I(\boldsymbol{x}_K), \psi_I(\boldsymbol{x}_L), \psi_I(\boldsymbol{x}_M)$ and $\psi_I(\boldsymbol{x}_N)$ $(I = 1, \cdots, NP)$ are assumed to be zero when the nodes are located in the external region of a RK function support as shown in Fig. 3 (b). The displacement of eq. (49) can be rewritten in matrix form as

$$\boldsymbol{v}^h_1 = \boldsymbol{N}_1 \boldsymbol{V}_1 = \boldsymbol{c}, \tag{50}$$

where $\boldsymbol{v}^h_1 = \{v_{1K} \quad v_{1L} \quad v_{1M} \quad v_{1N}\}^T$ is the displacement vector and $\boldsymbol{V}_1 = \{v_{11} \quad \cdots \quad v_{1NP}\}^T$ is the coefficient vector in terms of the RKs. $\boldsymbol{c}$ is an enforced value vector on the edge. When the edge is fixed, the vector $\boldsymbol{c}$ becomes a zero vector. $\boldsymbol{N}_1$ is a matrix of the RKs. The matrix can be written as

$$\boldsymbol{N}_1 = \begin{bmatrix} \psi_1(\boldsymbol{x}_K) & \cdots & \psi_{NP}(\boldsymbol{x}_K) \\ \psi_1(\boldsymbol{x}_L) & \cdots & \psi_{NP}(\boldsymbol{x}_L) \\ \psi_1(\boldsymbol{x}_M) & \cdots & \psi_{NP}(\boldsymbol{x}_M) \\ \psi_1(\boldsymbol{x}_N) & \cdots & \psi_{NP}(\boldsymbol{x}_N) \end{bmatrix}. \tag{51}$$

Performing a fundamental operation with pivot for eq. (50), we can separate the DOFs into dependent DOFs and independent DOFs. Eq. (50) can be rewritten as

$$[\boldsymbol{I},\ \boldsymbol{T},\ \boldsymbol{0}] \begin{Bmatrix} \boldsymbol{V}_D \\ \boldsymbol{V}_I \\ \boldsymbol{V}_O \end{Bmatrix} = \tilde{\boldsymbol{c}}, \tag{52}$$

where $\boldsymbol{I}$ is a unit vector, $\boldsymbol{T}$ is a matrix after the elimination process, and $\boldsymbol{0}$ is unrelated part of the enforcements. $\boldsymbol{V}_D$, $\boldsymbol{V}_I$ and $\boldsymbol{V}_O$ are vectors in terms of dependent DOFs, independent DOFs and the unrelated DOFs, respectively. And $\tilde{\boldsymbol{c}}$ is an enforced value vector after the rearranging. The rank of $\boldsymbol{V}_D$+$\boldsymbol{V}_I$+$\boldsymbol{V}_O$ is NP, and the $\boldsymbol{V}_D$ has same rank with the $\tilde{\boldsymbol{c}}$. By rearranging eq. (52), we obtain

$$\boldsymbol{V}_D = -\boldsymbol{T}\boldsymbol{V}_I + \tilde{\boldsymbol{c}}. \tag{53}$$

Dependent vector $\boldsymbol{V}_D$ can be represented by the superposition of tensor product $\boldsymbol{T}\boldsymbol{V}_I$ and vector $\tilde{\boldsymbol{c}}$.

3.2 Synchronization of node displacements/rotations

In the finite element analysis, the assumption of continuity of plating and periodicity of structures can be implemented by constructing tying relations between nodes; *i.e.*, some node displacements/rotations are synchronized with others. However, the RKs do not have

the so-called Kronecker delta property, and the treatment is thus slightly complicated. Here, we assume a tying relation on the right edge of the rectangular plate (Case 2) as shown in Fig. 3(c). We denote the four nodes along the edge as K', L', M' and N'. Additionally, the displacement in the x_1 direction can be defined as eq. (49). In this case, the nodes K', L', M' and N' always remain in straight line. The relation can be written as vector $\boldsymbol{v}_1'^h$:

$$\boldsymbol{v}_1'^h = \begin{Bmatrix} v^h_{1L'} - v^h_{1K'} \\ v^h_{1M'} - v^h_{1K'} \\ v^h_{1N'} - v^h_{1K'} \end{Bmatrix}, \tag{54}$$

where node K' is a master node and the others are slave nodes of the synchronization of DOFs. Displacement $v^h_{1L'}$, $v^h_{1M'}$ and $v^h_{1N'}$ are synchronized to $v^h_{1K'}$ so as to keep straight line. According to the relation in eq. (54), the displacement in the x_1 direction is expressed as

$$\boldsymbol{v}_1'^h = \boldsymbol{N}_1'\boldsymbol{V}_1' = \boldsymbol{c}', \tag{55}$$

where $\boldsymbol{c}'$ is the enforced value vector and $\boldsymbol{V}_1'$ is the coefficient vector for the x_1-direction component. To construct a tying relation, the enforced value $\boldsymbol{c}'$ is taken as a zero vector. The matrix $\boldsymbol{N}_1'$ can be written as

$$\boldsymbol{N}_1' = \begin{bmatrix} \psi_1(\boldsymbol{x}_{L'}) - \psi_1(\boldsymbol{x}_{K'}) & \cdots & \psi_{NP}(\boldsymbol{x}_{L'}) - \psi_{NP}(\boldsymbol{x}_{K'}) \\ \psi_1(\boldsymbol{x}_{M'}) - \psi_1(\boldsymbol{x}_{K'}) & \cdots & \psi_{NP}(\boldsymbol{x}_{M'}) - \psi_{NP}(\boldsymbol{x}_{K'}) \\ \psi_1(\boldsymbol{x}_{N'}) - \psi_1(\boldsymbol{x}_{K'}) & \cdots & \psi_{NP}(\boldsymbol{x}_{N'}) - \psi_{NP}(\boldsymbol{x}_{K'}) \end{bmatrix}. \tag{56}$$

We perform the fundamental operation with pivot of eq.(55). The relation between the dependent-node vector $\boldsymbol{V}_D'$ and independent-node vector $\boldsymbol{V}_I'$ is

$$\boldsymbol{V}_D' = -\boldsymbol{T}'\boldsymbol{V}_I' + \tilde{\boldsymbol{c}}', \tag{57}$$

where $\boldsymbol{T}'$ is the matrix after the fundamental operation and $\tilde{\boldsymbol{c}}$ is the enforced value vector after the elimination process. In this section, we only present the enforcement to keep a straight edge. Similarly, we can consider a periodic BC for synchronizing node displacements/rotations of adjacent edges of the rectangular plate.

3.3 Degeneration of the tangent stiffness matrix

The tangent stiffness matrix can be degenerated employing the relation of dependent DOFs and independent DOFs as shown in eq. (53) and (57). We derive a relation using the dependent-DOF vector $\boldsymbol{V}_D$ and independent-DOF vector $\boldsymbol{V}_I$ of eq. (53):

$$\boldsymbol{V} = \begin{Bmatrix} \boldsymbol{V}_D \\ \boldsymbol{V}_I \\ \boldsymbol{V}_O \end{Bmatrix} = \begin{bmatrix} \boldsymbol{I} & -\boldsymbol{T} & \boldsymbol{0} \\ \boldsymbol{0} & \boldsymbol{I} & \boldsymbol{0} \\ \boldsymbol{0} & \boldsymbol{0} & \boldsymbol{I} \end{bmatrix} \begin{Bmatrix} \tilde{\boldsymbol{c}} \\ \boldsymbol{V}_I \\ \boldsymbol{V}_O \end{Bmatrix} = \boldsymbol{C}\boldsymbol{V}_c, \tag{58}$$

where $\boldsymbol{C}$ is the transformation matrix. When the known vector $\tilde{\boldsymbol{c}} \neq \boldsymbol{0}$, the matrix of eq. (58) will be degenerated. Adopting the relation of eq. (58) to the virtual work principle in eq. (27), we have

$$\delta\boldsymbol{V}_c^T\boldsymbol{C}^T\boldsymbol{K}\boldsymbol{C}\boldsymbol{V}_c = \delta\boldsymbol{V}_c^T\boldsymbol{C}^T\boldsymbol{F} - \delta\boldsymbol{V}_c^T\boldsymbol{C}^T\boldsymbol{Q}. \tag{59}$$

Finally, we obtain

$$\boldsymbol{K}_c\boldsymbol{V}_c = \boldsymbol{F}_c - \boldsymbol{Q}_c, \tag{60}$$

where $\boldsymbol{K}_c(=\boldsymbol{C}^T\boldsymbol{K}\boldsymbol{C})$, $\boldsymbol{F}_c(=\boldsymbol{C}^T\boldsymbol{F})$ and $\boldsymbol{Q}_c(=\boldsymbol{C}^T\boldsymbol{Q})$ are the global tangent stiffness matrix, external force vector and internal force vector after the degeneration. The degeneration of the tangent stiffness matrix is time consuming. In this study, the node-by-node calculation is implemented in numerical code.

3.4 Evaluation of the MPC technique

When adopting the MPC technique for enforcing the essential BC and tying relation as mentioned in the previous section, displacements near the boundaries are violated. In this section, we examine the problem and propose an approach to improve the accuracy. The rectangular plate model and BCs shown in Fig. 3(a) are used in the validation. The size of the rectangular plate is 1000×1000 mm. Using the BCs, we obtain a linear exact solution (the so-called constant strain condition) in the finite element analysis. The RK models are shown in Fig. 4 (a), (b) and (c). Hereafter, we refer to the models as Models A1, B1 and C1, respectively. Model A1 is a regular distributed model. Models B1 and C1 are irregular distributed models. Boundary nodes of Model B1 are regular but those of Model C1 are irregular. The models have 121 nodes (11×11). A Voronoi cell is employed to automate the model generation. The parameter that determines the support of the kernel is $h = 1.15a$ (a is distance between nodes) in all cases.

To check the problem, differences between the exact solution of displacements u_1 along the underside ($x_2 = 0$) are shown in Fig. 5. The cubic spline function in eq. (5) is adopted as the original kernel function $\phi_{aI}(\boldsymbol{x})$. Although the exact solution is obtained at the both ends (x_1=0, 1000 mm), there is violation of displacements near the edges in all regular and irregular models. The width of the violation becomes small as the node density increases, but the error remains. The representation of eq. (53) is the same as that of eq. (50), and we can therefore obtain approximated displacements $\boldsymbol{v}_1^h$ in eq. (50) exactly along the edges using vectors $\boldsymbol{V}_I$ and $\boldsymbol{V}_D$. However, the vectors $\boldsymbol{V}_I$ and $\boldsymbol{V}_D$ do not have a one-to-one relation, because matrix $\boldsymbol{T}$ in

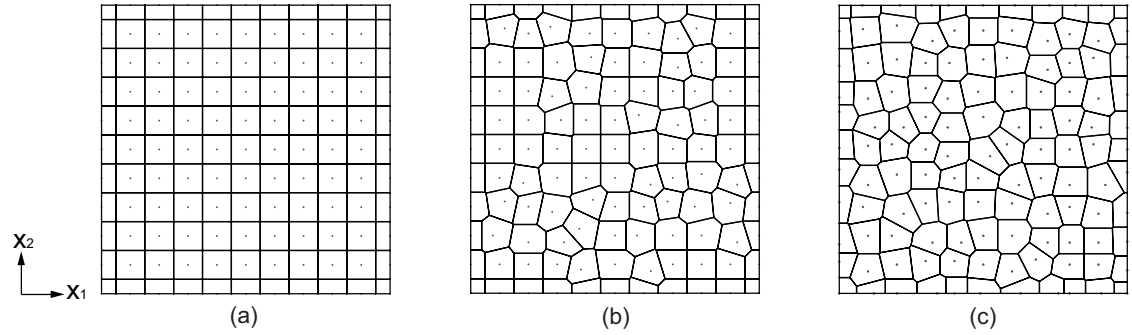

Fig. 4 RK models (11×11 nodes) [(a) Model A1, (b) Model B1, (c) Model C1]

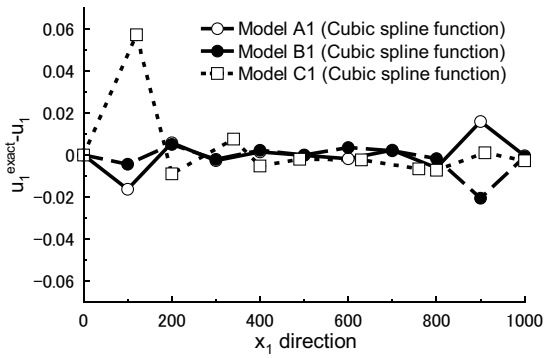

Fig. 5 Error in displacement u_1 along the x_1 direction ($x_2 = 0$) employing a cubic spline function ($h = 1.15a$)

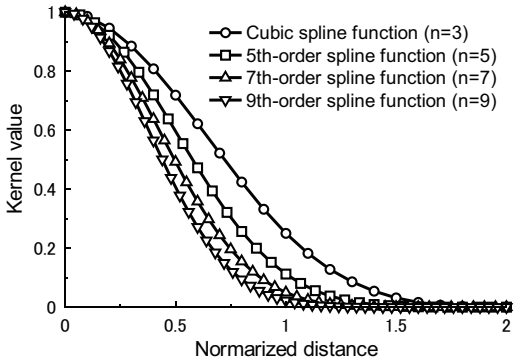

Fig. 6 Shape of n-th-order spline functions (n=3, 5, 7 and 9)

eq. (53) is non-regular. The solution then deteriorates near the edges after solving eq. (60).

We then propose an approach to improve the solution. A higher-order spline function is introduced as the original kernel function $\phi_{aI}(\boldsymbol{x})$. Here, we assume the n-th-order spline function consists of an n-th-order piecewise polynomial function. The one-dimensional n-th-order spline function can be written as a power series [44]:

$$\phi^{(n)}(x) = \frac{1}{n!}\sum_{k=0}^{n+1}(-1)^k\ {}_{n+1}C_k(x-k)_+^n \tag{61}$$

$$x_+ = \max[0, x] \tag{62}$$

$$x_+^n = (x_+)^n, \tag{63}$$

where the function support is

$$supp\ \phi^{(n)} = [0, n+1]. \tag{64}$$

In this evaluation, fifth, seventh and ninth-order spline functions are adopted. The shapes of the spline functions are shown in Fig. 6. The support of the spline functions (n = 5, 7 and 9) is enlarged as the order increases, as shown in eq. (64). The support is scaled so as to coincide with the support size of the cubic spline function. To accurately integrate the tangent stiffness matrix using SCNI, 10-point Gauss quadrature is used when the higher order spline functions are adopted.

Differences between the exact solutions of displacements u_1 along the underside ($x_2 = 0$) are shown in Fig. 7 when adopting a ninth-order spline function. The amplitude of the violation is small compared with that in Fig. 5. Hence, the relation between the independent DOFs $\boldsymbol{V}_I$ and the dependent DOFs $\boldsymbol{V}_D$ improves when a higher-order function is adopted in generating the matrix $\boldsymbol{T}$. Stress norms (L_1-norm) of σ_{11} are compared in Fig. 8 for several RK models. The horizontal axis represents the use of the n-th-order spline function. Models A2 and B2 are regular and irregular models with 21×21 nodes, and Models A3 and B3 are regular and irregular models with 41 × 41 nodes. The models are presented in Fig. 9 (a), (b), (c) and (d), respectively. In the figures, the error uniformly converges when a higher-order spline function is adopted. Additionally, the error in the models with regularly distributed nodes (A1, A2, A3) is small compared with that in the models with irregular distributed nodes (B1, B2, B3). In addition, as the node density increases, the error uniformly converges. It is thus found that the adoption of the higher-order spline function reduces the error near the enforced boundary and is effective when the MPC technique is used to enforce the BCs in the meshfree approach.

Error distributions of stress σ_{11} obtained employing the cubic spline function are shown in Fig. 10 (a), (b)

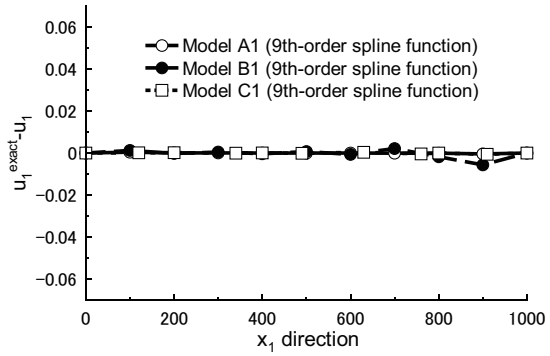

Fig. 7 Error in displacement u_1 along the x_1 direction ($x_2 = 0$) employing a ninth-order spline function ($h = 1.15a$)

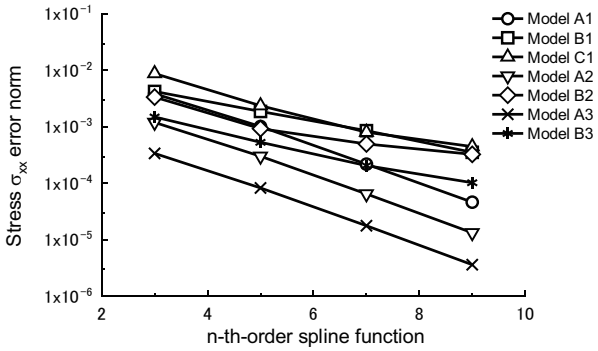

Fig. 8 Error norm of stress σ_{11} ($h = 1.15a$)

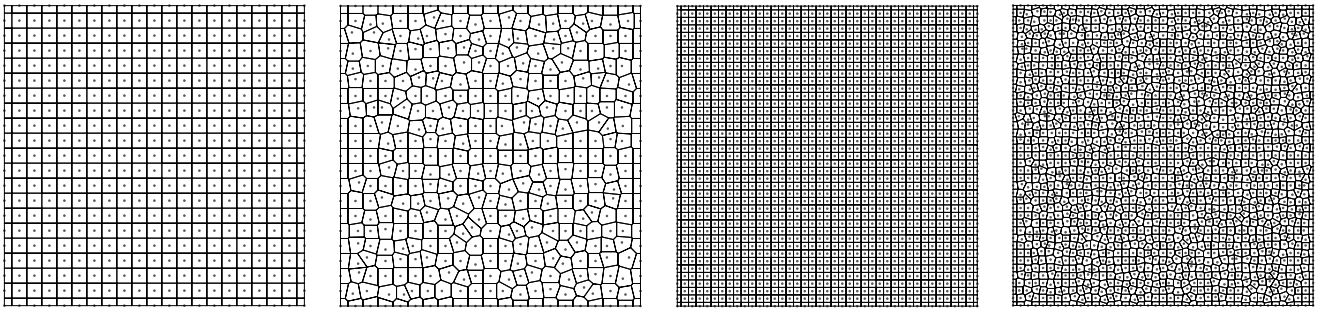

Fig. 9 RK models (21×21 and 41×41 nodes) [(a) Model A2, (b) Model B2, (c) Model A3, (d) Model B3]

Table 2 Maximum error (%) of stress σ_{11} ($h = 1.15a$)

(%)

	n=3	n=5	n=7	n=9
Model A1	1.70E+00	7.45E-01	1.37E-01	4.92E-02
Model B1	5.55E+00	2.44E+00	1.22E+00	7.06E-01
Model C1	7.07E+00	2.91E+00	1.21E+00	7.14E-01
Model A2	1.75E+00	7.36E-01	1.35E-01	4.92E-02
Model B2	6.11E+00	2.90E+00	1.30E+00	1.24E+00
Model A3	1.76E+00	7.34E-01	1.35E-01	4.92E-02
Model B3	8.16E+00	2.42E+00	7.12E-01	5.11E-01

Table 3 Maximum error (%) of stress σ_{11} ($h = 1.30a$)

(%)

	n=3	n=5	n=7	n=9
Model A1	2.24E+00	5.88E-01	1.74E-01	1.16E-01
Model B1	3.33E+00	3.66E+00	3.10E+00	2.18E+00
Model C1	8.29E+00	5.54E+00	3.08E+00	2.07E+00
Model A2	2.23E+00	6.02E-01	1.72E-01	1.16E-01
Model B2	4.02E+00	3.15E+00	2.34E+00	1.35E+00
Model A3	2.25E+00	6.04E-01	1.71E-01	1.16E-01
Model B3	5.35E+00	4.04E+00	2.07E+00	1.15E+00

and (c) for Models A1, B1 and C1, respectively. The error is located on the enforced boundaries. The error in the irregular distributed model is greater than that in the regular distributed model. Fig. 11 (a), (b) and (c) presents the error in stress σ_{11} when employing the ninth-order spline function. The amplitude of the error is small in all cases. Table 2 presents the maximum errors for Models A1, B1, C1, A2, B2, A3 and C3 for different orders of spline functions (n=3, 5, 7 and 9). The support size $h = 1.15a$ is used in the literature, and numerical results of $h = 1.30a$ are also presented to check how the support size affects the solution. The maximum error of stress σ_{11} is presented in Table 3. As the function support size increases, the error is inclined to increase. Although the maximum stress error also uniformly converges when a higher-order spline function is adopted, more than 1% error remains in the analysis of Model B2 in Table 2. The error occurs locally on the boundary region near the nodes distributed with high irregularity. Because the matrix $\boldsymbol{T}$ in eq. (53) is non-regular, the solution is sensitively affected by the irregularity of the node distribution near the boundary compared with other enforcement techniques, such as the penalty method and Lagrange multiplier. Hence, further research is needed in the analysis of a model with a highly irregular node distribution, and it should address the adoption of the MPC technique in regions of high stress concentration such as at a hole edge or near a crack tip.

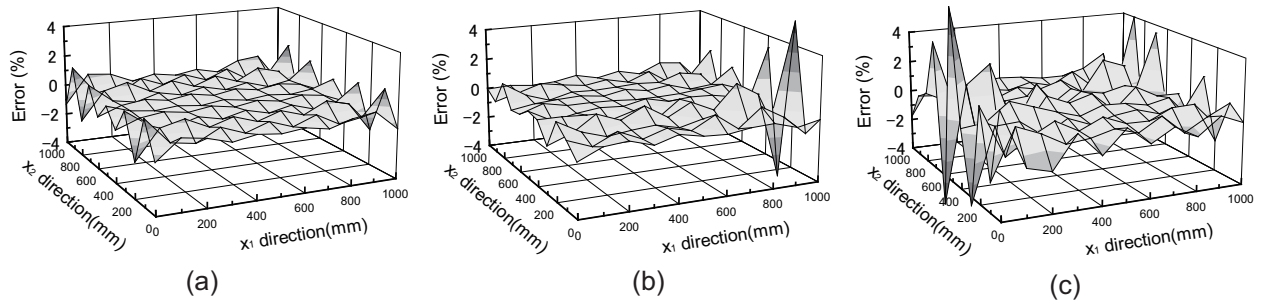

Fig. 10 Error distribution of σ_{11} (Cubic spline function, $h = 1.15a$) [(a) Model A1, (b) Model B1, (c) Model C1]

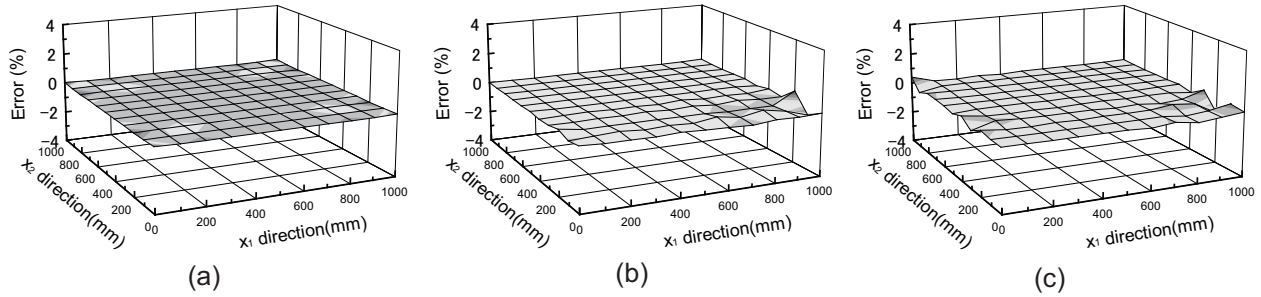

Fig. 11 Error distribution of σ_{11} (Ninth-order spline function, $h = 1.15a$) [(a) Model A1, (b) Model B1, (c) Model C1]

However, the global error norm uniformly converges as the node density increases as seen in Fig. 8. The error due to the inconsistency is therefore small compared with the global accuracy.

4 Numerical examples

Geometrical nonlinear analyses of plates and buckling analysis of a rectangular plate and stiffened plate structure are demonstrated as numerical examples. Validation and accuracy are discussed for the formulation of the plate bending analysis and the enforcement of the MPC technique. In the analysis, cubic, fifth-order, seventh-order and ninth-order spline functions are adopted as the original kernel function and the function support is set as $h = 1.15a$. Young's modulus is 206 GPa and Poisson's ratio is ν =0.3 in all cases.

4.1 Geometrical nonlinear analysis of plates

Bending analyses of a rectangular plate with geometrical nonlinearity are performed. The size of the rectangular plate is 1000×1000 mm. The plate thickness t_h is assumed as 10 mm. RK models A1, A2 and A3 (regularly distributed nodes) and B1, B2 and B3 (irregularly distributed nodes) are adopted. The node locations and the Voronoi cell diagrams correspond to the illustrations in Fig. 4 (a), (b) and 9 (a)-(d), respectively. Each node has five DOFs $(u_1^p, u_2^p, w, \beta_1, \beta_2)$. Analyses employing two BCs are performed; one analysis is of a simply supported model and the other is of a clamped edge model. Fig. 12 (a) is a schematic illustration of the simply supported model. In the analysis, all deflection components on the four edges are fixed. Additionally, the underside edge of the plate (x_2=0) is fixed in the x_2 direction and the left edge (x_1=0) is fixed in the x_1 direction. The other two edges are enforced with a tying relation considering the in-plane displacement of the edges in their perpendicular direction to be uniform. All rotational components are free. Fig. 12 (b) is an illustration of the clamped edge model. In the analysis of the clamped edge model, all components are fixed along all edges. The MPC technique is introduced to enforce both the essential BCs and tying relation.
In both analyses, uniform pressure is applied to the top of the plate and increased to 2.0 MPa. Geometrical nonlinear analyses are performed using MSC.Marc for the simply supported and clamped edge models as reference solutions. In the analyses, the rectangular plate is equally divided into 100×100 rectangular elements. A bilinear quadrilateral thick shell element (element no.75) is adopted [45]. The element is an assumed strain type element in order to avoid shear locking of bending and it has 6 DOFs per node. The numbers of DOFs are 605(A1, B1), 2205(A2, B2), and 8405(A3, B3). In the reference solution 61206 DOFs are used.

Pressure-deflection curves for the simply supported model and clamped edge model are shown in Fig. 13 and 14, respectively. In these figures, analysis results for RK

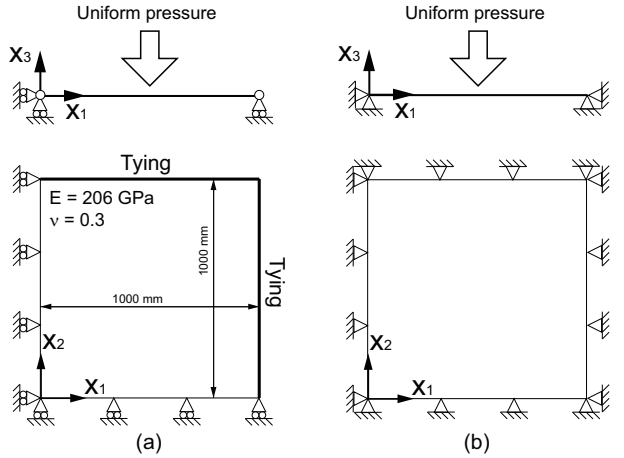

Fig. 12 Analysis model for the plate bending problem [(a) Simply supported model, (b) Clamped edge model]

models A3 and B3 employing a cubic spline function and ninth-order spline function are shown. Good results are obtained for both regular and irregular models compared with the reference solutions. The error in maximum deflection in the final step is evaluated in Fig. 15 for the RK models (A1, A2, A3) employing cubic, fifth-order, seventh-order and ninth-order spline functions. The error is constantly converges in all cases. Convergence for the clamped edge model is slower than that for the simply supported model. Furthermore, stress

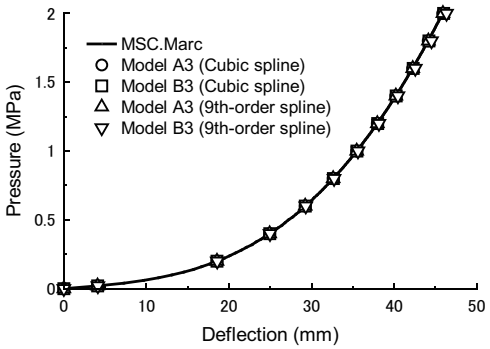

Fig. 13 Pressure-deflection curves (Simply supported model)

distributions of the plate in the final step are compared for the analyses with the cubic spline function and ninth-order spline function. Fig. 16 presents the mid-surface nominal stresses S_{11} and S_{22} along the x direction (x_2=500 mm) for RK models A3 and B3. These stresses are compared with the MSC.Marc results. Because the convergence of the clamped edge model analyses is slow as shown in Fig. 15, stress distributions of a finer model (61x61 nodes) are presented in Fig. 17. The 61x61-node regular and irregular models are respectively called models A3' and B3'. The results for the regular (A3') and irregular (B3') models are in good

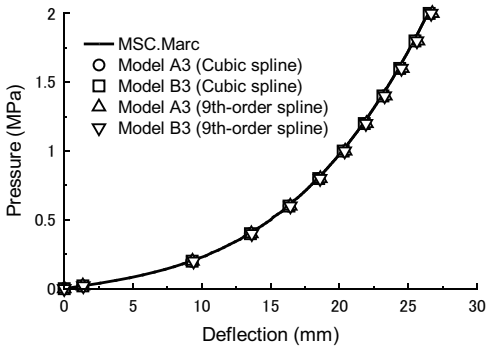

Fig. 14 Pressure-deflection curves (Clamped edge model)

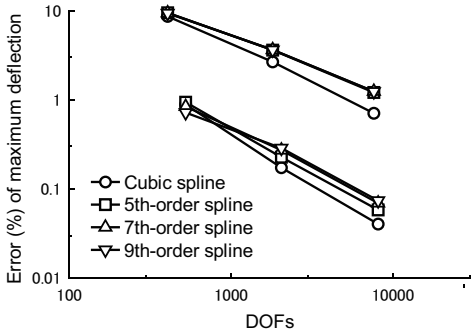

Fig. 15 Error (%) in the maximum deflection in the final step (Regularly distributed model)

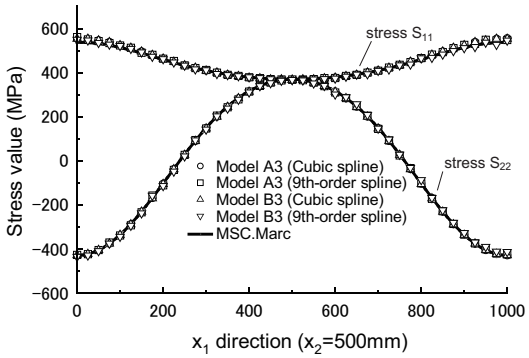

Fig. 16 Stress distribution of the simply supported model along the x_1 direction (x_2=500 mm)

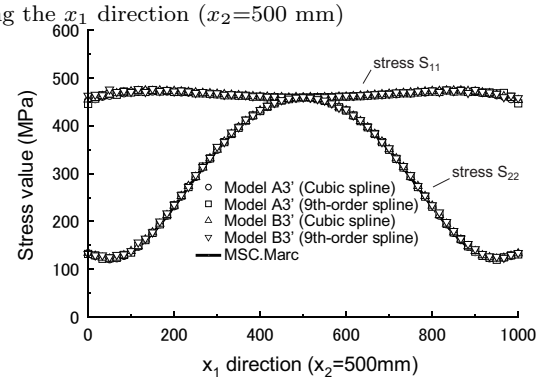

Fig. 17 Stress distribution of the clamped edge model along the x_1 direction (x_2=500 mm, 61×61 Model A3', B3')

agreement with the reference solution. The numerical results show that the plate bending analysis using an RK and SCNI obtain high-accuracy deformation/stress results and that the approach is effective in plate bending analysis including geometrical nonlinearity.

In the previous chapter, we mentioned that the adoption of the MPC technique cannot pass the so-called patch test exactly, and we proposed improving the solution by employing a higher-order spline function as the original kernel function. However, the effect of the violation was small compared with the global accuracy. This can be discussed in terms of the maximum deflection and overall stress distributions of this example. Other numerical examples are investigated in the next section.

4.2 Buckling/post-buckling analysis of a rectangular plate

In the analyses carried out in the previous section, bending deformation was dominant. Here, we solve the problem of both bending and membrane deformation to verify the enforcements of the MPC technique. RK models A1, A2, A3, B1, B2 and B3 are also used.

Large deflection analyses of a rectangular plate subjected to uniaxial thrust are carried out to evaluate the buckling/post-buckling behaviors. Illustrations of the rectangular plate model and the analysis procedures are presented in Fig. 18 (a) and (b). Plate thickness t_h is assumed to be 5 mm. The BCs and tying relation are the same as those of the simply supported model solved in section 4.1. The analysis is carried out into two steps. Uniform pressure is applied to the top of plate in the first step in Fig. 18 (a), and uniaxial thrust is adopted in the consecutive steps as shown in Fig. 18 (b). Step 1 is thus considered as the introduction of the initial imperfection. Analyses with three uniform pressures are adopted; the maximum deflection A_0 in step 1 is set to be A_0/t_h=0.01, 0.05 and 0.1. A point load is adopted and increased to 2.0e5 N on the tying edge (x_1=1000 mm). Analyses are also performed employing cubic, fifth-order, seventh-order and ninth-order spline functions. The same analysis is performed using MSC.Marc to provide reference solutions. To check the sensitivity of the initial imperfection in the buckling/post-buckling behaviors, analysis with very small pressure is also carried out using MSC.Marc. In this case, the pressure is set such that A_0/t_h=1e-4 in step 1.

The numerical results are shown in Fig. 19 and 20 for Model A3 (regular model) and Model B3 (irregular model) respectively. Additionally, a convergence study is carried out for the regular models (A1, A2 and A3) employing the cubic, fifth-order, seventh-order and ninth-order spline functions in Fig. 21. The numerical results are in good agreement with the reference solutions in all cases. Additionally, the numerical results converge as a finer RK model is adopted. It is found that the sensitivity of initial imperfections is well represented in the buckling analyses. Stress distributions S_{11} and S_{22} along the x_1 direction (x_2=500 mm) in the

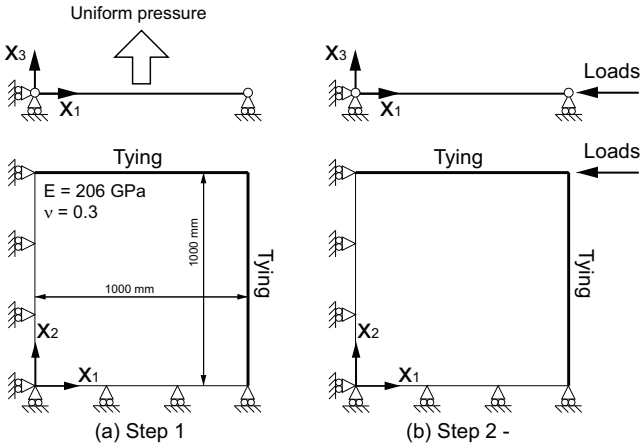

Fig. 18 Model for the buckling analysis of a rectangular plate [(a) Step 1 (Uniform pressure), (b) Step 2 (Point loads)]

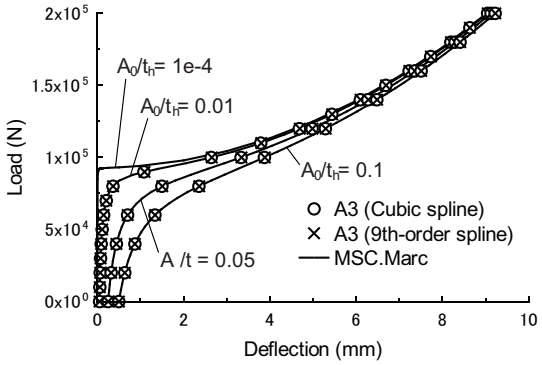

Fig. 19 Load-deflection curve for Model A3 (regularly distributed model)

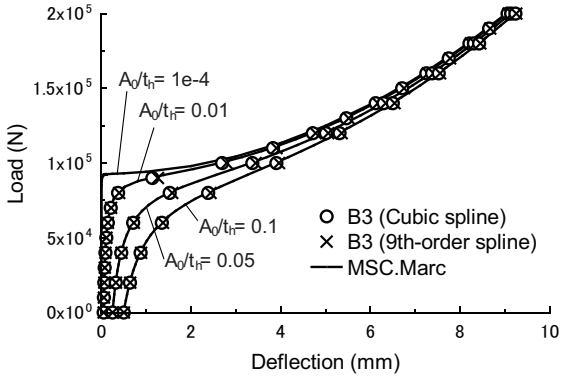

Fig. 20 Load-deflection curve for Model B3 (irregularly distributed model)

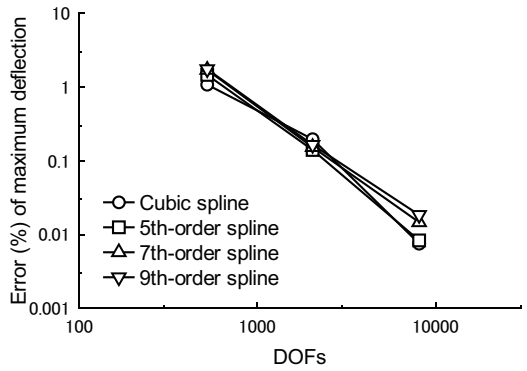

Fig. 21 Convergence study (A_0/t_h=0.01)

final step are shown in Fig. 22 for Models A3 and B3. Good results are obtained compared with the reference solution.

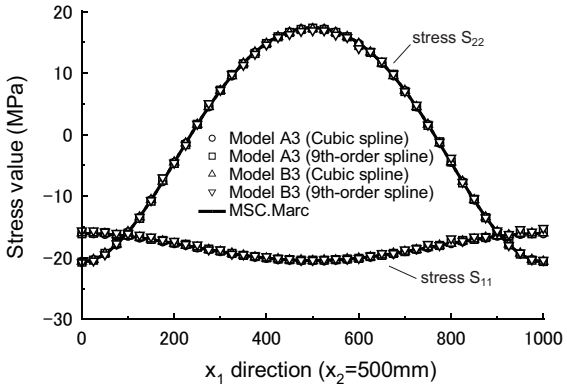

Fig. 22 Stress distribution along the x_1 direction (x_2=500 mm)

To compare the present method with FEM in terms of the accuracy, the stress distributions S_{11} and S_{22} are presented in Fig. 23. Model A2 is chosen and the FEM model has the same number of nodes. In addition, the results on middle part of the plate and the edge are focused. Although both results show good agreement with the reference solution, the accuracy of the present method is superior to that of the FEM in the comparison. These results imply the effectivity of the proposed approach.

As was the case in section 4.1, there are also little differences between the analyses with the cubic spline function and the higher-order spline function in the global stress evaluation of the structural analysis. The inexactness of the MPC technique affects the local stress-level approach, but the effect is small relative to the global error in examples 4.1 and 4.2.

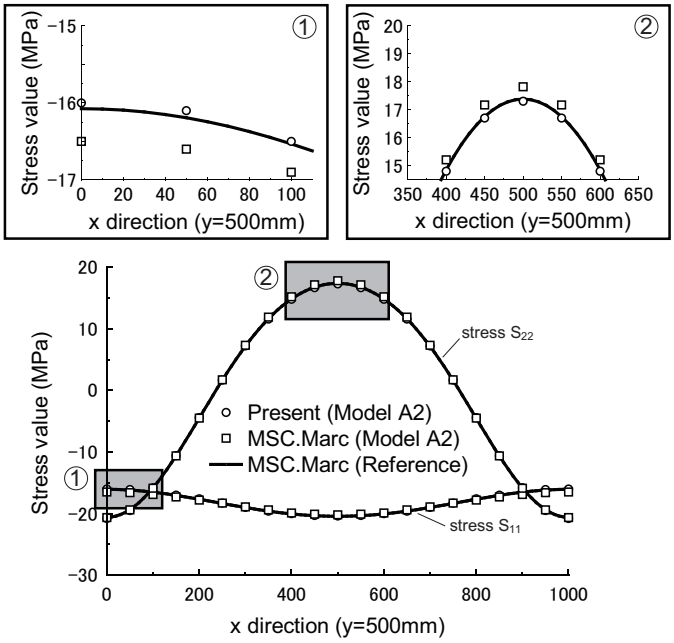

Fig. 23 Stress distribution along the x_1 direction (x_2=500 mm, Model A2)

4.3 Buckling/post-buckling analysis of a stiffened plate

Large deflection analysis of a stiffened plate structure is demonstrated to evaluate the buckling/post-buckling behaviors. The solutions of MSC.Marc are used as reference solutions. The stiffened plate structure is often used in ships and ocean structures to prevent buckling of the structural members [46]. The stiffened plate structure model is shown in Fig. 24 (a). The model is periodic structure that is stiffened by longitudinal girders and transverse frames. The distance between adjacent transverse frames is a=1000 mm and that between adjacent longitudinal girders is b=500 mm. The aspect ratio a/b is 2.0. Plate thickness t_h is assumed to be 10 mm. In structural analysis of the stiffened plate structure, the shaded region ($IJKL$) in Fig. 24 (b) is used. The model is the so-called double-span double-bay model. RK models A4 and B4 are shown in Fig. 25(a) and (b). The models have 1891 (61×31) nodes (9455 DOFs). The reference solution uses 30906 DOFs. In Fig. 25(a) and (b), Voronoi cells are the calculation domain of SCNI and triangles in the Voronoi cells are the domain of SSCI, where deflections are fixed. The domains are also employed to automate the model generation.

In this case, there are two buckling half waves in the loading direction. The maximum deflection of the wave A_0 is assumed to be 0.1 mm (A_0/t_h=0.01). The waves are adopted as the initial configuration in the analy-

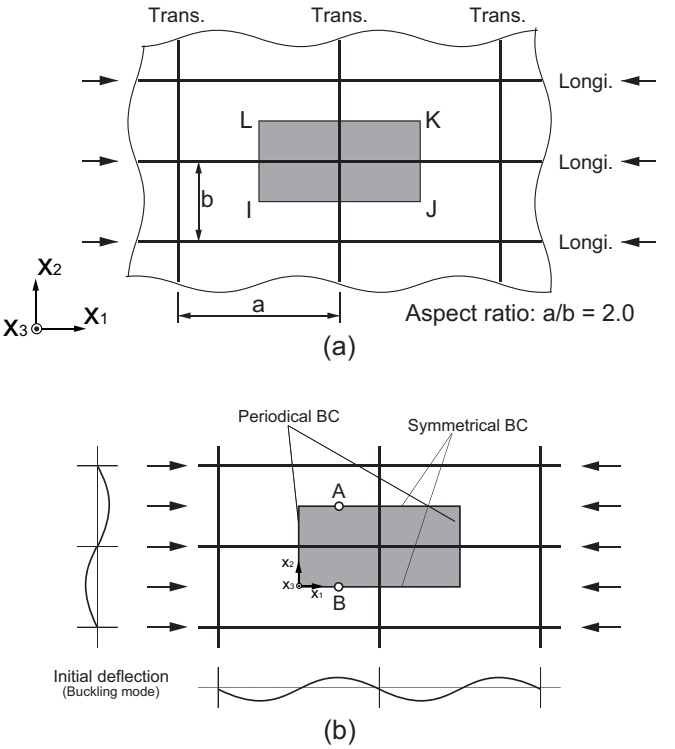

Fig. 24 Analysis model for buckling analysis of a stiffened plate [(a) Stiffened plate structure (a/b=2.0), (b) Double-bay double-span model]

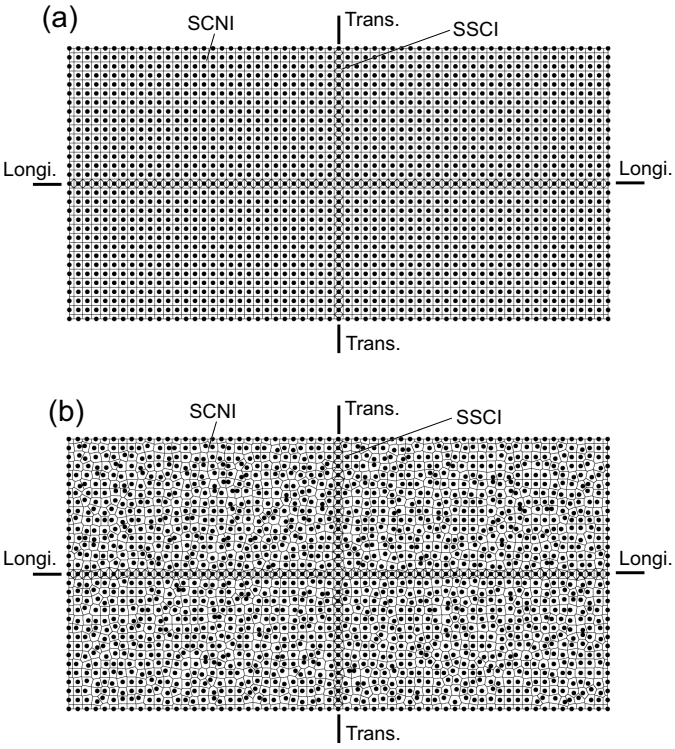

Fig. 25 RK models (61×31 nodes)[(a) Model A4, (b) Model B4]

sis using MSC.Marc calculation. On the other hand, in the proposed approach, the waves are adopted as a displacement mode $\boldsymbol{U}_0$. $\boldsymbol{U}_0$ is a function of the coordinates so as to represent the waves. Assuming that the model is under the equivalent condition when the mode of buckling half waves $\boldsymbol{U}_0$ is applied, there are external forces equal to the internal nodal forces. That is, the initial condition of the analysis is

$$ {}^{t_0}_{0}\boldsymbol{K}\boldsymbol{U}_0 = {}^{t_0}_{0}\boldsymbol{F} - {}^{t_0}_{0}\boldsymbol{Q} = \boldsymbol{0}, \tag{65} $$

where t_0 is the time step for the shape of waves adopted and ${}^{t_0}_{0}\boldsymbol{K}$, ${}^{t_0}_{0}\boldsymbol{F}$ and ${}^{t_0}_{0}\boldsymbol{Q}$ are the tangent stiffness matrix, external works vector and internal works vector at time step t_0, respectively. Therefore, it is little but the effect of initial stresses is considered in the analysis. The analysis is carried out after the condition of eq.(65) is satisfied. BCs are described in Fig. 24 (b). Deflections are fixed along the longitudinal girders and transverse frames. Considering continuity and periodicity of the structure, which depend on the buckling half waves, a periodic BC is enforced along lines IL and JK and a symmetrical BC is enforced along lines IJ and KL. As the load cases, there is into two steps. Uniform pressure is applied to the top of the plate in the first step assuming water pressure (w_p), and uniaxial thrust is adopted in subsequent steps. Four cases of uniform pressure are considered (w_p = 0.0, 0.1, 0.2, 0.3 MPa) and a point load is adopted and increased to 2.5e6 N on the tying edge (x_1=1000 mm). Analyses are performed employing cubic, fifth-order, seventh-order and ninth-order spline functions.

The numerical results are shown in Fig. 26-29 for Model A4 (regular model) and Model B4 (irregular model). The numerical results are in good agreement with the reference solutions in all cases. In Fig. 26 and 27, it is found that the effect of water pressure is well represented in the analyses, and it is also found that the deformations depend on the initial buckling half waves even if water pressure was applied. Stress distributions S_{11} and S_{22} along the x_1 direction (the line KL, x_2=500 mm) in the final step are shown in Fig. 28 and 29 for Models A4 and B4. In Fig. 28, the case that water pressure is not applied is presented. In Fig. 29, the case that water pressure is 0.3 MPa is presented. Good results are obtained compared with the reference solution, there are also little differences between the solutions with cubic spline function and with ninth-order spline function. Moreover, the stress is periodic in the both ends of the line KL because of the enforcement of the periodic BC, the validity of the adoption of the MPC technique as the enforcement of periodic BC was presented.

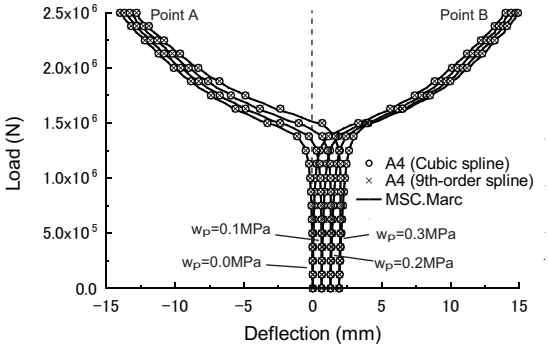

Fig. 26 Load-deflection curve for Model A4 (regularly distributed model)

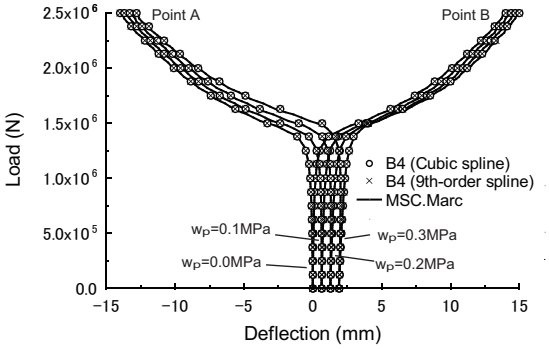

Fig. 27 Load-deflection curve for Model B4 (irregularly distributed model)

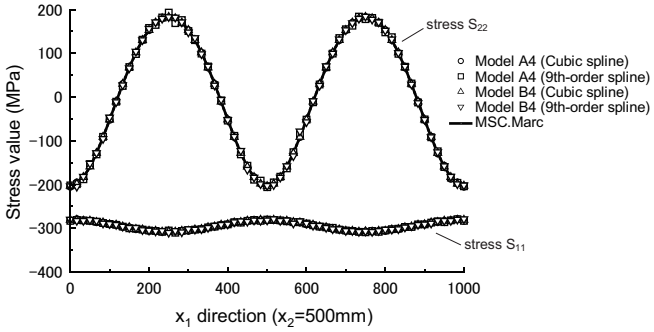

Fig. 28 Stress distribution along the x_1 direction (w_p=0.0MPa, x_2=500 mm)

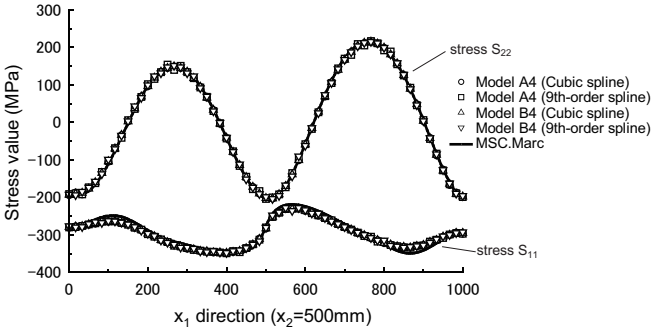

Fig. 29 Stress distribution along the x_1 direction (w_p=0.3MPa, x_2=500 mm)

5 Conclusion

This paper presented the buckling/post-buckling analysis of plate structures using RK approximation and treatment of the boundary condition considering the continuity/periodicity of structures. In-plane and bending deformations were coupled and the total Lagrangian formulation is used to represent general plate bending with geometrical nonlinearity. The representation of bending deformation is based on Mindlin-Reissner plate theory, and the plate is shear-deformable in the present approach. Nodal integration was performed by SCNI and SSCI so as to satisfy the integration constraint. The MPC technique was used for the essential BC and synchronization of DOFs. When adopting the MPC technique to enforce the essential BC and tying relation, displacements and stresses near the boundaries are violated. The problem of adopting the MPC technique was discussed for stress-level evaluation and we proposed an approach to improve the solution. A higher-order spline function was introduced as the original kernel function, which reduced the amplitude of the violation. However, the violation is a local problem near the enforced boundaries; the effect of the violation was small in terms of the global accuracy in patch test. The problem was also examined by numerical examples. Simple-bending and buckling/post-buckling analyses of a rectangular plate and stiffened plate structure were presented as numerical examples to demonstrate the validity of the proposed approach. The results indicated good agreement with a reference solution obtained using commercially available FEM software. Hence, we should consider issues arising when applying the MPC technique to problems such as a stress concentration near boundaries, which was not so much the case in the examples presented in this paper. Moreover, the BCs such as periodic or essential BCs were well adopted by the MPC technique; the technique is an effective means with witch to solve problems of plate bending or buckling/post-buckling behavior.

Analyses of the stiffened plate structure were carried out for numerical examples, but longitudinal girders and transverse frames were not modeled in the analyses. We will solve the stiffened plate structure considering plate and plate conbinations using the MPC technique in future work.

Acknowledgements This research was partially supported by JKA through its promotion funds from KEIRIN RACE. A part of the present research conducted by Satoyuki Tanaka was financially supported by The Research Council of Norway (RCN) through the Yggdrasil mobility programme.

References

1. Nayroles B., Touzot G. and Villon P., 1992, Generalizing the finite element method: diffuse approximation and diffuse elements, Computational Mechanics, 10, pp. 307-318.
2. Belytschko T., Lu Y. Y. and Gu L., 1994, Element-free Galerkin Methods, International Journal for Numerical Methods in Engineering, 37, pp. 229-256.
3. Liu W. K., Jun S. and Zhang Y. F., 1995, Reproducing kernel particle methods, International Journal for Numerical Methods in Fluids, 20, pp. 1081-1106.
4. Durate C. A. and Oden J. T., 1996, An *h-p* adaptive method using clouds, Computer Methods in Applied Mechanics and Engineering, 139, pp. 237-262.
5. Atluri S. N. and Zhu T., 1998, A new meshless local Petrov-Galerkin (MLPG) approach in computational mechanics, Computational Mechanics, 22, pp. 117-127.
6. Belytschko T., Kronggauz Y., Organ D. and Fleming M., 1996, Meshless methods: an overview and recent developments, Computer Methods in Applied Mechanics and Engineering, 139, pp. 3-47.
7. Li S. and Liu W. K., 2002, Meshfree and particle methods and their applications, Applied Mechanics Review, 55, pp. 1-34.
8. Babuška I., Banerjee U. and Osborn J. E., 2003, Survey of meshless and generalized finite element methods: a unified approach, Acta Numerica, 12., pp. 1-125.
9. Li S. and Liu W. K., 2004, Meshfree Particle Methods, Springer.
10. Liu G. R., 2009, Mesh free methods: moving beyond the finite element method, 2nd edition, CRC Press, Coca Raton.
11. Li S., Hao W. and Liu W. K., 2000, Numerical simulations of large deformation of thin shell structures using meshfree methods, Computational Mechanics, 25, pp. 102-116.
12. Qian D., Eason T., Li S. and Liu W. K., 2008, Meshfree simulation of failure modes in thin cylinders subjected to combined loads of internal pressure and localized heat, International Journal for Numerical Methods in Engineering, 76, pp. 1159-1184.
13. Gato C., 2010, Meshfree analysis of dynamic fracture in thin-walled structures, Thin-Walled Structures, 48, pp. 215-222.
14. Krysl P. and Belytschko T., 1996, Analysis of thin plates by the element-free Galerkin method, Computational Mechanics, 17, pp. 26-35.
15. Krysl P. and Belytschko T., 1996, Analysis of thin shells by the element-free Galerkin method, International Journal of Solids and Structures, 33, pp. 3057-3080.
16. Long S. Y. and Atluri S. N., 2002, A meshless local Petrov-Galerkin method for solving the bending problem of a thin plate, Computer Modeling in Engineering and Sciences, 3, pp. 53-63.
17. Wang D. and Chen J. S., 2004, Locking-free stabilized conforming nodal integration for meshfree Mindlin-Reissner plate formulation, Computer Methods in Applied Mechanics and Engineering, 193, pp.1065-1083.
18. Wang D. and Chen J. S., 2008, A Hermite reproducing kernel approximation for thin-plate analysis with sub-domain stabilized conforming integration, International Journal for Numerical Methods in Engineering, 74, pp. 368-390.
19. Wang D. and Lin Z., 2010, Free vibration analysis of thin plates using Hermite reproducing kernel Galerkin meshfree method with sub-domain stabilized conforming integration, Computational Mechanics, 46, pp. 703-719.
20. Wang D. and Lin Z., 2011, Dispersion and transient analyses of Hermite reproducing kernel Galerkin meshfree method with sub-domain stabilized conforming integration for thin beam and plate structures, Computational Mechanics, 48, pp. 47-63.
21. Chen J. S. and Wang D., 2006, A constrained reproducing kernel particle formulation for shear deformable shell in Cartesian coordinates, International Journal for Numerical Methods in Engineering, 68, pp. 151-172.
22. Liu Y., Hon Y. C. and Liew K. M., 2006, A meshfree Hermite-type radial point interpolation method for Kirchhoff plate problems, International Journal for Numerical Methods in Engineering, 66, 1153-1178.
23. Noguchi H., Kawashima T. and Miyamura T., 2000, Element free analyses of shell and spatial structures, International Journal for Numerical Methods in Engineering, 47, pp. 1215-1240.
24. Wang D. and Sun Y., 2011, A galerkin mashfree method with stabilized conforming nodal integration for geometrically nonlinear analysis of shear deformable plates, International Journal of Computational Methods, 8, pp. 685-703.
25. Liew K. M., Chen X. L. and Reddy J. N., 2004, Mesh-free radial basis function method for buckling analysis of non-uniformly loaded arbitrary shaped shear deformable plates, Computer Methods Applied Mechanics and Engineering, 193, pp. 205-224.
26. Liew K. M., Peng L. X. and Kitipornchai S., 2006, Buckling analysis of corrugated plates using a mesh-free Galerkin method based on the first-order shear deformation theory, Computational Mechanics, 38, pp. 61-75.
27. Bui T. Q., Nguyen M. N. and Zhang Ch., 2011, Buckling analysis of Reissner-Mindlin plates subjected to in-plane edge loads using a shear-locking-free and meshfree method, Engineering Analysis with Boundary Elements, 35, pp. 1038-1053.
28. Liew K. M., Peng L. X. and Kitipornchai S., 2007, Geometric non-linear analysis of folded plate structures by the spline strip kernel particle method, International Journal for Numerical Methods in Engineering, 71, pp. 1102-1133.
29. Lu H., Cheng H. S., Cao J. and Liu W. K., 2005, Adaptive enrichment meshfree simulation and experiment on buckling and post-buckling analysis in sheet metal forming, Computer Methods Applied Mechanics and Engineering, 194, pp. 2569-2590.
30. Rabczuk T., Areias P. M. A. and Belytschko T., 2007, A meshfree thin shell method for non-linear dynamic fracture, International Journal for Numerical Methods in Engineering, 72, pp. 524-548.
31. http://www.qhull.org/
32. Chen J. S., Wu C. T., Yoon S. and You Y., 2001, A stabilized conforming nodal integration for Galerkin meshfree methods, International Journal for Numerical Methods in Engineering, 50, pp. 435-466.
33. Chen J. S., Yoon S. and Wu C. T., 2002, Non-linear version of stabilized conforming nodal integration for Galerkin mesh-free methods, International Journal for Numerical Methods in Engineering, 53, pp. 2587-2615.
34. Cho J. Y., Song Y. M. and Choi Y. H., 2008, Boundary locking induced by penalty enforcement of essential boundary condition in mesh-free methods, Computer Methods Applied Mechanics and Engineering, 197, pp. 1167-1183.
35. Belyschko T., Organ D. and Krongauz Y., 1995, A coupled finite element - element free Galerkin method, Computational Mechanics, 17, pp. 186-195.
36. Krongauz Y. and Belyschko T., 1996, Enforcement of essential boundary conditions in meshless approximations using finite elements, Computer Methods Applied Mechanics and Engineering, 131, pp. 133-145.

37. Hegen D., 1996, Element-free Galerkin methods in combination with finite element approaches, Computer Methods Applied Mechanics and Engineering, 135, pp. 143-166.
38. Chen J. S., Pan C., Wu C. T. and Liu W. K., 1996, Reproducing kernel particle methods for large deformation analysis of nonlinear structures, Computer Methods Applied Mechanics and Engineering, 139, pp. 195-227.
39. Chen J. S. and Wang H. P., 2000, New boundary condition treatments in meshfree computation of contact problems, Computer Methods Applied Mechanics and Engineering, 187, pp. 441-468.
40. Nagashima T., 2000, Development of a CAE system based on the node-by-node meshless method, Computer Methods Applied Mechanics and Engineering, 187, pp. 1-34.
41. Wu C. T., Koishi M., Skinner G. and Shimamoto H., 2008, A meshfree procedure for the microscopic simulation and design of rubber compounds and its application to multi-scale simulation of tires, Proceedings of WCCM8 and ECCOMAS 2008, pp. 1-2.
42. Noguchi H. and Zhang Z., 2007, Analysis of large deformation of rubber-filler structures under periodic boundary conditions using an enhanced meshfree method, Proceeding of the Computational Mechanics Conference, 20, pp. 661-662.
43. Liu W. K., Jun S., Li S. Adee J. and Belytschko T., 1995, Reproducing kernel particle methods for structural dynamics, International Journal for Numerical Methods in Engineering, 38, pp. 1655-1679.
44. Chui C. K. and Wang G. Z., 1991, A cardinal spline approach to wavelet, Proceeding of the American Mathematical Society, 113, pp. 785-793.
45. MSC.Marc 2005r3, User's Guide.
46. Fujikubo M., Yao T., Khedmati M. R., Harada M. and Yanagihara D., 2005, Estimation of ultimate strength of continuous stiffened panel under combined transverse thrust and lateral pressure Part 1: Continuous Plate, Marine Structures, 18, pp. 383-410.